POLITECNICO DI TORINO

Politecnico di Torino

Master Degree course in Mechatronic Engineering Software Technologies for Automation

Master Degree Thesis

System Propulsion Hardware-in-the-Loop for Fuel Cell Vehicles

Supervisors

Prof. Claudio Passerone

Antonio Vitale

Davide Milone

Candidate

Federica Liuzzi

Academic Year 2024-2025

Abstract

The automotive industry is becoming increasingly complex with the integration of advanced technologies such as electric vehicles, fuel cell vehicles, and autonomous driving functions. To ensure that these systems operate correctly and safely, rigorous and accurate testing is essential throughout all stages of development. Hardware-in-the-Loop (HIL) technology plays a crucial role in meeting this demand by providing an effective real-time method for testing and validating control systems.

In the automotive context, vehicle control systems, such as engine control units or propulsion systems, are integrated with simulated models of the rest of the vehicle and its operational environment. This approach allows for testing and validating control systems in a safe and controlled environment, reducing the need for expensive and potentially hazardous initial physical tests.

This thesis, developed in collaboration with Kineton, an automotive consultancy based in Turin, documents the implementation of a Hardware-in-the-Loop solution for the propulsion system of fuel cell vehicles, focusing on a project led by Stellantis. It provides an explanation of how the HIL system is set up and details the operational framework. The study delves into the development of a subsystem model within the complex architecture of the fuel cell system, specifically, a Simulink model of the hydrogen tank. This model is crucial for analyzing the dynamics and operational characteristics of hydrogen storage in fuel cell vehicles and has been tested and validated as part of the larger fuel cell model. To ensure accuracy and reliability, the study briefly examines how the model's outputs compare to real-world data. This comparison is achieved through the analysis of real signals obtained from in-vehicle testing, focusing on communication between the Hydrogen Power Unit (HPU) and critical components, such as the Hydrogen Control Module (HCM) and the Electric Vehicle System Management (EVSM).

By examining these aspects, the research aims to demonstrate how HIL technology can improve the effectiveness and efficiency of the development process while ensuring the safety and reliability of innovative propulsion systems in automotive applications.

Contents

List of Figures

Chapter 1

Introduction

The automobile sector is swiftly progressing towards sustainable technology, encompassing electric vehicles (EVs), fuel cell vehicles (FCVs), and autonomous systems. As these technologies advance, the assurance of their safety, efficiency, and dependability becomes progressively crucial. In this context, Hardware-in-the-Loop (HIL) simulations have become vital instruments, offering dynamic, real-time testing environments that accurately replicate actual vehicle operations. This methodology mitigates development risks and expenses, while markedly improving the safety and reliability of these systems. This thesis examines the design and configuration of a Hardware-in-the-Loop (HIL) system tailored for the propulsion systems of fuel cell vehicles, offering a thorough platform for the meticulous testing and validation of essential vehicle components under simulated conditions that replicate real-world operations. The HIL setup comprises many organized phases: identifying the Device Under Test (DUT), constructing the simulation model in Simulink, designing the wiring harness with Napkin software, setting I/O modules via Configuration Desk, and performing a series of open-loop tests. One of the critical procedures, "flashing," is vital in this HIL configuration as it installs the necessary software onto each control unit within the system. The incorporation of essential real nodes, including the Fuel Cell Power System (FCPS), Battery Management System (BMS), and Electric Vehicle Control Unit (EVCU), within the Hardware-in-the-Loop (HIL) environment offers considerable benefits compared to only simulated nodes. Evaluating real components in simulated driving scenarios facilitates a more precise assessment of the system's functionality, aiding in the early detection of hardware and software problems. The genuine nodes undergo stringent testing to verify their simulated behaviors, ensuring the system's realism and operational precision.

The inclusion of actual hardware components within the HIL environment enables more authentic and meaningful testing, enhancing test results' reliability and reducing

the risks and costs associated with later stages of development. Additionally, analyzing the network topologies within the vehicle is a vital part of the HIL setup. Optimizing the communication and functional interactions among the Electronic Control Units (ECUs) ensures efficient data flow and improves overall system performance. This network analysis is crucial as it details how nodes, sensors, and actuators are interconnected, supporting the integrated functionality of the vehicle's network.

A significant part of this research involved developing a Simulink model for the hydrogen storage tank, critical for understanding the dynamics of hydrogen storage and its impact on the vehicle's operational efficiency and safety. The model simulates the state changes of hydrogen under various conditions and incorporates detailed thermal analyses that account for heat transfer through conduction and convection. These features are essential for accurately predicting the tank's response to external and internal thermal variations.

The hydrogen tank model was integrated in the laboratory into a more complex FCPS model within the broader HIL simulation environment. This integration allowed for extensive testing of the tank model's interactions with other system components, including the fuel cell stack, Battery Management System (BMS), and Electric Vehicle Management System (EVMS). The comprehensive laboratory setup provided a complete architecture for testing and refining the hydrogen tank model under conditions that closely mimic actual vehicle operations.

To validate the hydrogen tank model, real-world data was collected during on-road testing of fuel cell vehicles. This validation phase was critical for aligning simulation outputs with actual data, ensuring the model's accuracy and operational reliability. Data analysis was performed offline using CANalyzer, focusing on the signals transmitted and received by the fuel cell control unit across two CAN systems. This analysis was instrumental in assessing the precise behavior of the fuel cell system under various operational conditions, identifying discrepancies between simulated results and actual data.

The insights gained from real-world data were essential for refining the Simulink model, allowing precise adjustments of simulation parameters to replicate how the vehicle's fuel cell system responded to different driving conditions. Integrating real nodes into the HIL setup, validated with rigorous real-world data analysis, has significantly enhanced the overall testing process. This realistic framework not only allows for identifying potential operational issues but also enables the testing of physical characteristics and failure modes that simulations alone might not reveal.

Ultimately, this research highlights the profound impact of advanced HIL simulations on the development process for fuel cell vehicle systems, underscoring their potential to improve vehicle safety, efficiency, and reliability. By facilitating complex scenario testing

within a controlled environment, HIL simulations reduce development time and costs associated with physical prototypes, enriching the field of automotive engineering and promoting the adoption of fuel cell technology for more sustainable automotive solutions.

The use of fossil fuels dates back to the late 18th century and saw a significant increase during the second half of the 20th century, when petroleum emerged as the primary energy source. Rapid global economic growth and the industrial revolution increased energy demand from industries; until the 1950s, this demand was mainly met through coal use.

Currently, a large part of the world's energy demand relies on gasoline, petroleum, kerosene, and naphtha because of their compactness, ease of transport, storage capabilities, and relatively low cost. However, fossil fuels contribute to climate change due to their pollution, non-renewability, and greenhouse gas emissions from combustion. The increase in energy demand has led to depletion of available fuel reserves and subsequent price increase. This new economic landscape, coupled with increasing environmental awareness, has encouraged the development of environmentally friendly and less polluting energy supply methods.

Road transport is a significant source of emissions. Battery electric and hybrid vehicles offer an alternative to internal combustion engine (ICE) vehicles in this sector. The widespread adoption of purely electric transportation faces challenges such as high vehicle prices, longer charging times compared to ICE vehicles, and the relatively low number of charging infrastructures. Another factor limiting the use of these vehicles is "range anxiety," which is the fear that the vehicle may not have sufficient range to reach a destination. Addressing these challenges, the concept of a range extender has been introduced. A range extender is an auxiliary power unit (APU) that provides additional energy to help power the vehicle's battery. It typically combines a small ICE or a fuel cell with a battery, allowing to extend the vehicle's range while maintaining lower emissions compared to conventional ICE vehicles. Unlike vehicles with range extenders, fuel cell technology converts hydrogen into electricity, producing only water vapor and heat as byproducts: it offers the advantage of producing no polluting substances during the hydrogen conversion process.

Before diving into the specifics of Hardware-in-the-Loop (HIL) simulations, which this thesis will detail, it is essential to understand these alternative propulsion technologies. HIL simulations play a crucial role in testing and optimizing vehicle systems, including electric and hybrid propulsion systems like batteries and fuel cells, under controlled conditions that mimic real-world scenarios.

The thesis is structured as follows:

- Chapter 1: Introduces the Hardware-in-the-Loop (HIL) simulation system.
- Chapter 2: Analyzes the operational principles and architecture of fuel cell technology by focusing on the propulsione scope.
- Chapter 3: Focuses on the analysis of the documentation provided by Stellantis and the practical activities required to set up the Hardware-in-the-Loop (HIL) system.
- Chapter 4 - This chapter conducts an in-depth evaluation of the high-pressure hydrogen tank along with its regulatory frameworks. It focuses on the intricate modeling of thermal behaviors and the computation of energy balances, which are pivotal for grasping and forecasting the operational dynamics of the system.
- Chapter 5: provides an explanation about three diagnostic procedures employed within the Simulink model. It outlines the different features and effectiveness of each technique in observing and mitigating temperature and pressure variations across several simulation settings.
- Chapter 6: it introduces additional simulation variables, including state valves and power dependencies, and analyzes their effects on system performance. The simulations assist in delineating the operating dynamics and pinpointing potential areas for enhancement.
- Chapter 7 includes the summary about the results.

1.1 HIL in automotive industry

In the automotive industry, HIL (Hardware-in-the-Loop) is used in various fields. Specifically, in the area of **safety systems**, HIL is employed to ensure the reliability of critical vehicle functions, such as braking systems and driver assistance. For example, thanks to HIL technology, it's possible to test the ABS braking system by simulating potentially dangerous and complex scenarios to evaluate how the ABS would respond. Similarly, the proper functioning of the vehicle's stability control system (ESC) can be checked through simulations that replicate scenarios where the vehicle might lose traction. Lastly, ADAS (Advanced Driver Assistance Systems) can be subjected to simulations and tests to verify the reliability of features such as cruise control or automatic emergency braking.

In the field of **infotainment and connectivity systems**, Hardware-in-the-Loop tests and simulations are performed on various vehicle system components. One key area is user interfaces that include touchscreens, buttons and voice commands that are used by drivers or passengers to interact with the vehicle's systems. Another important area is the

navigation systems, such as GPS and mapping tools. Additionally, HIL technology is very important for the Vehicle-to-vehicle connectivity (V2V) systems. These systems allow the communication between vehicles for sharing information regarding speed, position, and potential road hazards. The goal of these tests is to ensure that all components interact smoothly and are user-friendly for the end-user. The entire system must operate continuously, without interruptions, increasing both user comfort and safety.

HIL also plays a crucial role in the development and **validation of autonomous vehicles**. It aids in testing autonomous driving algorithms, sensors, and actuators, which are essential for the safe and efficient operation of self-driving cars.

This thesis, however, will specifically focus on the application of HIL in the field of **propulsion systems**. It will delve into the testing and optimization of electric motors, battery management systems, and fuel cells. By using HIL technology, the aim is to enhance the performance and reliability of these propulsion components, contributing to the advancement of electric and fuel cell vehicles.

1.1.1 HIL advantages

HIL is particularly important in the automotive industry for several reasons:

- Safety and Reliability: Testing critical systems, such as braking or driver assistance systems, in a controlled environment reduces the risk of accidents and allows potential issues to be identified and resolved before implementation in real vehicles.
- Cost Reduction: Using HIL saves on costs related to building physical prototypes and subsequent modifications, offering a more economical and flexible testing method.
- Accelerated Development Cycle: HIL tests can be conducted in parallel with product development, allowing for rapid iterations and faster identification of issues. This accelerates the time-to-market of new vehicles and technologies.
- Realistic Testing Conditions: HIL simulators can replicate a wide range of operating conditions and driving scenarios, including extreme and rare ones, which are difficult to reproduce in road or track tests.

1.2 V-shaped Workflow

Hardware-in-the-loop is one of the steps of the V-model (Verification and Validation model), that is a development model that illustrates how verification and validation

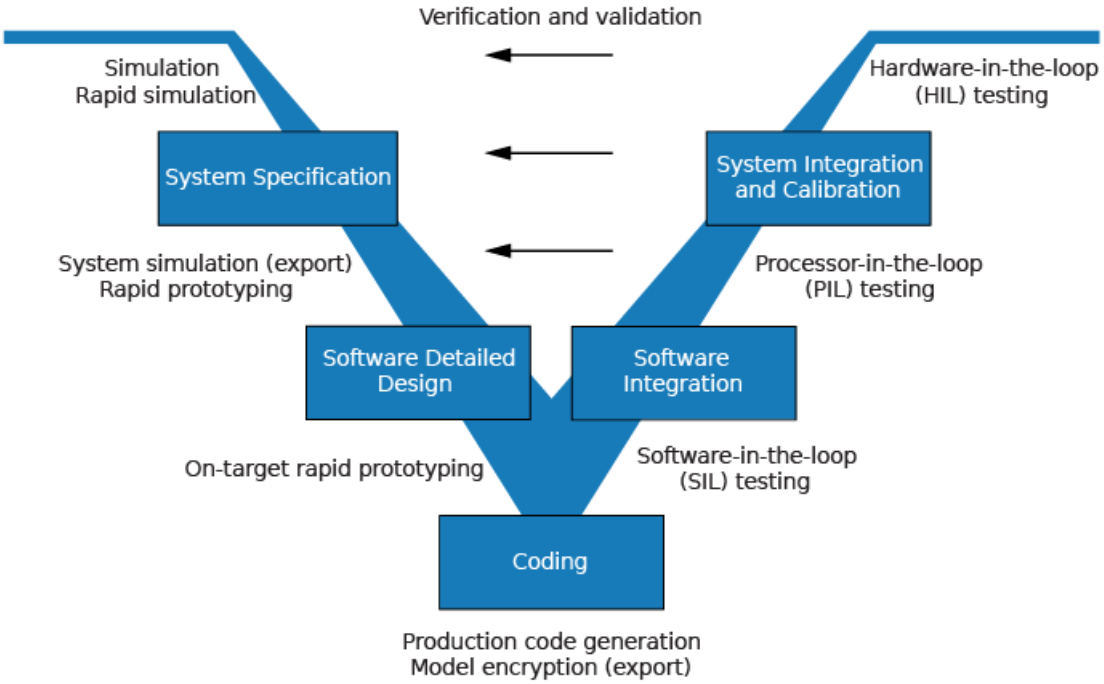

Figure 1.1. V-cycle

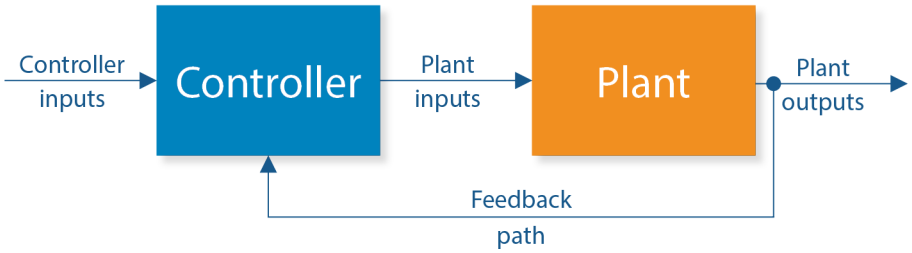

Figure 1.2. Control system

activities relate to each stage of the development lifecycle. The left side of the V represents the decomposition of requirements and creation of system specifications, while the right side represents the integration and verification of the system components (Figure 1.1).

Following the steps of the V-cycle, the ultimate goal is to achieve a reactive system where the target system is represented by an ECU (Electronic Control Unit) and the plant is represented by a simulator. In this setup, the ECU runs the controller, while the simulator is connected to it, providing status information and receiving commands from the ECU (Figure 1.2).

The design flow step permits different types of analysis:

- Model-in-the-loop test (MIL): This test is performed during the first steps of V-shaped design flow that include the System specification and Software Design. The initial phase of the control system development process involves creating a detailed mathematical model of the plant, representing the system to be controlled (System specification). Concurrently, a model of the controller is designed to interact with the plant model (Software Detailed Design). By applying inputs to the plant model, it is possible to observe and analyze the plant's responses. Similarly, the controller model allows for setting reference points and statuses to evaluate the commands it generates. Subsequently, the plant and controller models are integrated to simulate the behavior of the complete control system (System Simulation). This simulation phase is crucial for refining and perfecting the controller. The plant simulation is tested iteratively until it demonstrates satisfactory performance. At the same time, the controller model undergoes rigorous testing and adjustments. The combined simulation assesses whether the control system can achieve the desired set points, maintain the specified sampling time, and keep control errors within acceptable limits.

- Optimization and code generation: Following the refinement of the controller model, the next step (Coding) involves translating this model into executable code. This translation process includes multiple validation steps to ensure the code achieves the intended outcomes accurately. The generated code can vary depending on the chosen transformation rules and methodologies.

  During this phase, the focus is on code generation and optimization, ensuring that the code is detailed and tailored for the specific processor used in the target embedded system. This results in platform-dependent code, necessitating optimization for efficient operation on the designated hardware.

- Software-in-the-loop test (SIL): It is performed during the edge steps of V-shaped design flow. Software in the Loop (SIL) testing is conducted at this stage. SIL testing involves co-simulating the controller code with the plant model on a PC. This step verifies that the code maintains the intended control behavior, despite potential precision losses when switching from floating-point to integer calculations.

- Processor-in-the-loop test (PIL): The next phase involves running the controller software on the actual embedded hardware intended for the final application, known as Processor in the Loop (PIL) testing. During this phase, the plant model runs

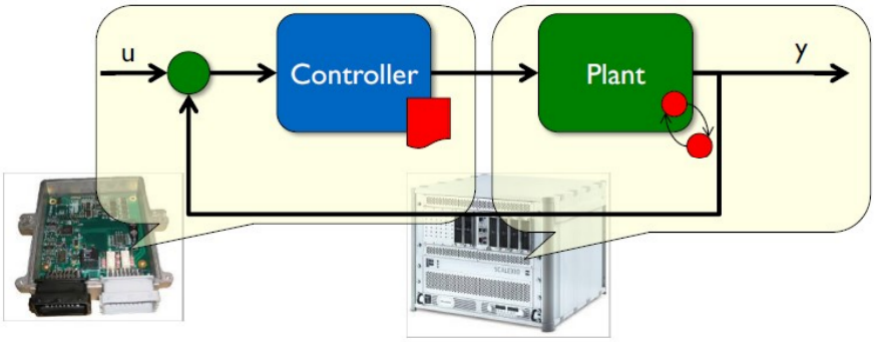

Figure 1.3. HIL model loop

on the PC while the controller code executes on the real embedded hardware. This setup validates that the platform-specific code functions correctly.

A critical aspect at this stage is addressing timing discrepancies, as the simulation on the PC may run faster or slower than the real plant, meaning real-time conditions are not yet being met.

- Hardware-in-the-loop test (HIL): Part of the model runs in a real-time simulator and part may exists as physical driver (ECU), good for testing interactions with HW and real-time performance. This phase involves connecting the controller to emulation hardware that runs the plant model in real time. This setup closely mimics the final application environment (Figure 1.3).

  HIL testing represents the most expensive and complex validation step, as it requires running the simulation in real time rather than simulation time. Additionally, the bypass technique may be used, wherein specific functions are executed on rapid prototyping hardware, distributing the controller algorithm between the ECU and the prototyping hardware. This approach is necessary when direct modification of the ECU software is not feasible.

1.3 HIL system components

The HIL system consists of a simulator that replicates real-world conditions, an electronic control unit (ECU) that processes the signals, and a device under test (DUT) that interacts with the ECU. All components are connected through a hardware and software interface. A host PC then manages the entire setup by coordinating the simulation and analyzing the results (Figure 1.4).

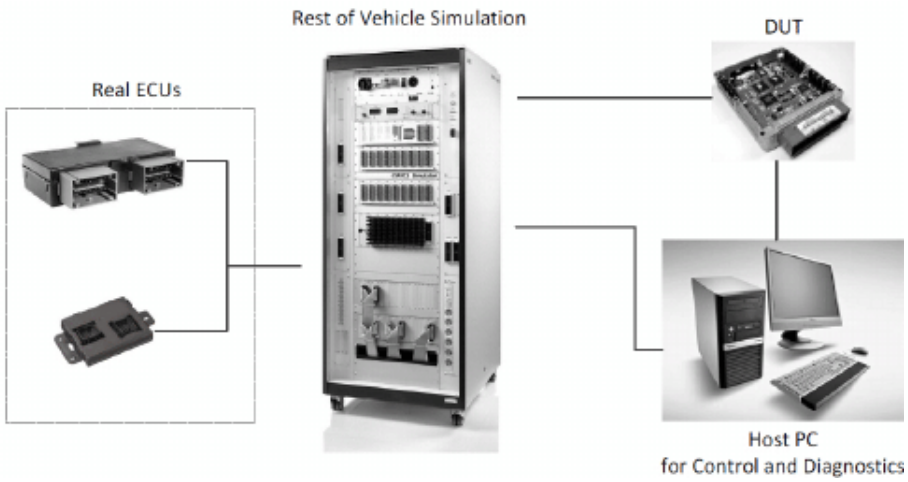

Figure 1.4. HIL system

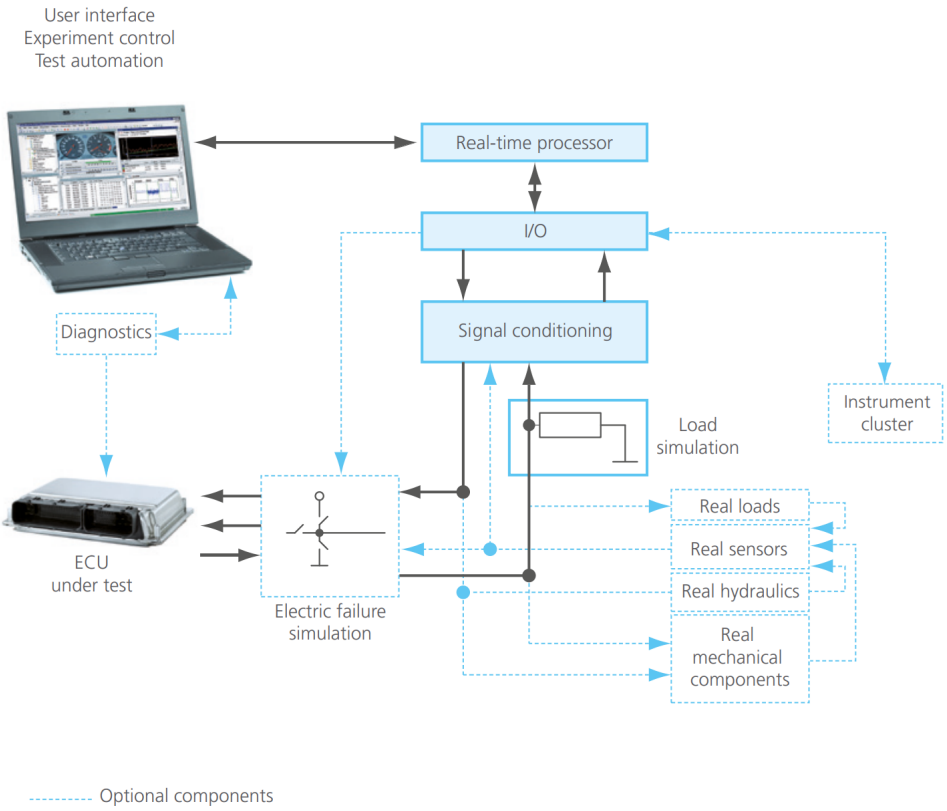

Figure 1.5. Components in HIL system

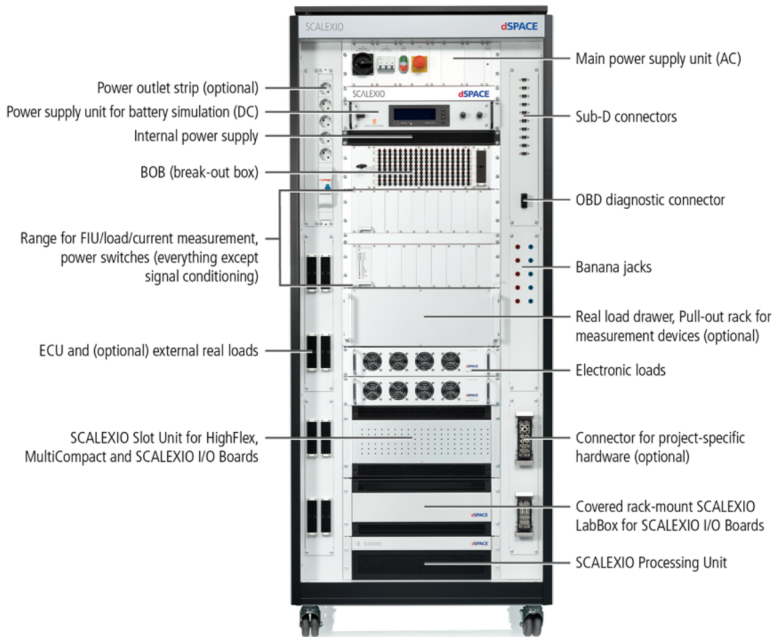

Figure 1.6. HIL simulator

The core hardware components of a Hardware-in-the-Loop (HIL) system include several key elements. These elements are shown in the (Figure 1.5).

In the project, the HIL simulator (Figure 1.6) used is the dSpace Scalexio customized system. Since it is intended to meet specific customer needs, the simulator is designed to provide a wide range of adaptation and configuration options. The main features of the SCALEXIO customized system are the following [8]:

- **Real-time processing system**: it is an integral part of the simulator and is a dedicated hardware component responsible for running real-time simulations. The real-time processore is based on an industrial PC with an Intel Core i7 processor and a real-time operating system (RTOS). It connects the host PC via Ethernet and its main function is to manage real-time simulations, while the host PC is used for configuring, monitoring, and controlling the simulator.

- **Host PC running Windows®**: This PC is used to interact with the real-time processor, letting users run software for experiments, modeling, and implementation. It uses fast network cards (like Gigabit Ethernet) to ensure quick and smooth communication with the hardware.

- **I/O boards**: They are essential for managing various analog and digital signals,

Figure 1.7. DS2680 board

including those that require fast, engine-angle-synchronous inputs for accurate sensor simulation and actuator measurement. These boards may include built-in signal conditioning and protection circuits to adapt to different electrical system voltages. In the dSPACE SCALEXIO system context, four **DS2680 boards** are used(Figure 1.7). These boards are MultiCompact units, offering all the necessary I/O channels for hardware-in-the-loop (HIL) simulation of transmission or vehicle dynamics ECUs: channels for voltage supply, channel for signal measurement, channels for signal generation and specific channel for lambda probe simulation.

- **Bus system**: in a vehicle, Electronic Control Units (ECUs) are interconnected and exchange data through various bus systems such as CAN, LIN. Within a hardware-in-the-loop (HIL) setup, some of these networks are simulated to accurately replicate the behaviour of the absent ECUs. This purpose is typically achieved by using specialized I/O boards, which are frequently equipped with FPGAs.

- **Management of Electrical Loads**: ECUs manage various electrical devices, such as valves, motors, relays, and injectors, known collectively as loads. In a HIL system, these loads can be either the actual physical components or their electrical equivalents. The ECU's diagnostic system monitors these loads for issues like short circuits or disconnections and reacts accordingly, either by taking action or alerting the driver. In many cases, a resistor can be used to simulate a load. However, if the load's behavior changes dynamically, such as the varying resistance in a headlamp, the HIL system may need to include the real load or use an electronic simulation controlled by the real-time system.

- **Fault Simulation in Electrical Systems**: HIL systems often incorporate fault simulation units to replicate electrical issues like short circuits, open circuits, or loose connections. These units can generate various fault conditions using either

relays or semiconductor switches, depending on the testing requirements. Faults can be introduced manually or through automated test scripts.

- **Integration of Real Components**: In some scenarios, accurately simulating ECU behavior requires the use of real components. This is particularly true for loads that are complex or resource-intensive to replicate electronically. Depending on the testing scenario, real components might be used in simple setups or more complex test benches.

- **Dynamic Power Supply Simulation**: Simulating the vehicle's electrical system, including the battery, requires power supplies capable of adjusting voltage levels dynamically, as specified by the HIL system. This is especially important for testing scenarios that involve voltage variations, such as during a truck jump-start or when simulating the voltage drop that occurs when an engine starts.

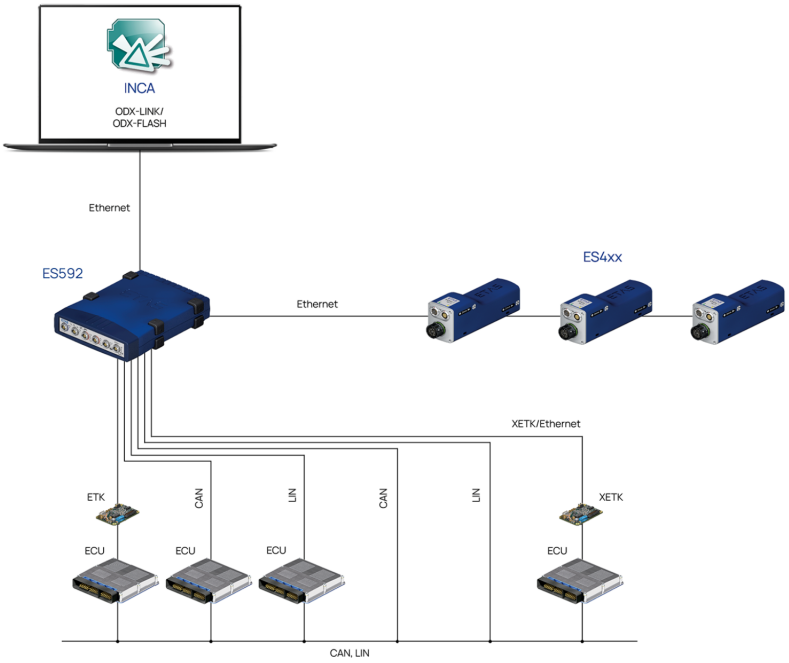

Figure 1.8. ETAS

- **ETAS**: The ES592 Interface Module offers one ETK connection, along with two CAN and two LIN interfaces. It connects to the PC via an Ethernet port, and the PC manages the interaction between the simulator and the ETAS module. It also includes two additional Ethernet ports to connect and synchronize with XETK

ECUs or other measurement modules. The calibration and acquisition software, INCA, runs on the PC, allowing it to communicate with the module and coordinate the testing and calibration processes. The main functions of the ETAS are the real-time calibration of ECU parameters, acquisition of data during system operation, simulation of scenarios, optimization of ECU behaviour in order to increase efficiency, safety and performance (Figure 1.8).

Chapter 2

Fuell Cell Vehicles

2.1 State of Art: Features and Applications

Fuel cells are highly efficient systems for generating electrical energy, owing to their energy characteristics and broad range of applications. They are used in various fields, including domestic and industrial cogeneration as well as traction applications. As cited in [18], Fuel cells come in various types (Figure 2.1), each distinguished by the kind of electrolyte they use. For instance, **Alkaline Fuel Cells (AFCs)** operate with potassium hydroxide as the electrolyte and function at temperatures between 60 and 120°C. Historically, they were popular in military and space missions, but their use has become limited today due to their need for pure feed gases and their sensitivity to contamination. In contrast, **Solid Oxide Fuel Cells (SOFCs)** employ a solid electrolyte and operate at much higher temperatures, ranging from 900 to 1000°C. This high-temperature operation is necessary to mantain adequate conductivity and enables SOFCs to be used primarily for energy generation with power outputs spanning from a few kilowatts to tens of megawatts. The materials used in these cells must be resilient to high temperatures.

Molten Carbonate Fuel Cells (MCFCs) use a molten carbonate electrolyte, making them well-suited for high-power cogeneration, with capabilities extending from several hundred kilowatts to tens of megawatts. **Polymer Electrolyte Fuel Cells (PEFCs)**, also known as Proton Exchange Membrane Fuel Cells (PEMFCs), utilize a polymer membrane that facilitates high proton conductivity. Operating at temperatures between 70 and 100°C, these cells are mainly designed for applications in vehicle traction and small-scale power generation, with power outputs ranging from 1 to 250 kW. **Phosphoric Acid Fuel Cells (PAFCs)** use a concentrated phosphoric acid solution as their electrolyte and have found widespread use in stationary applications, providing power outputs between 100 and 200 kW.

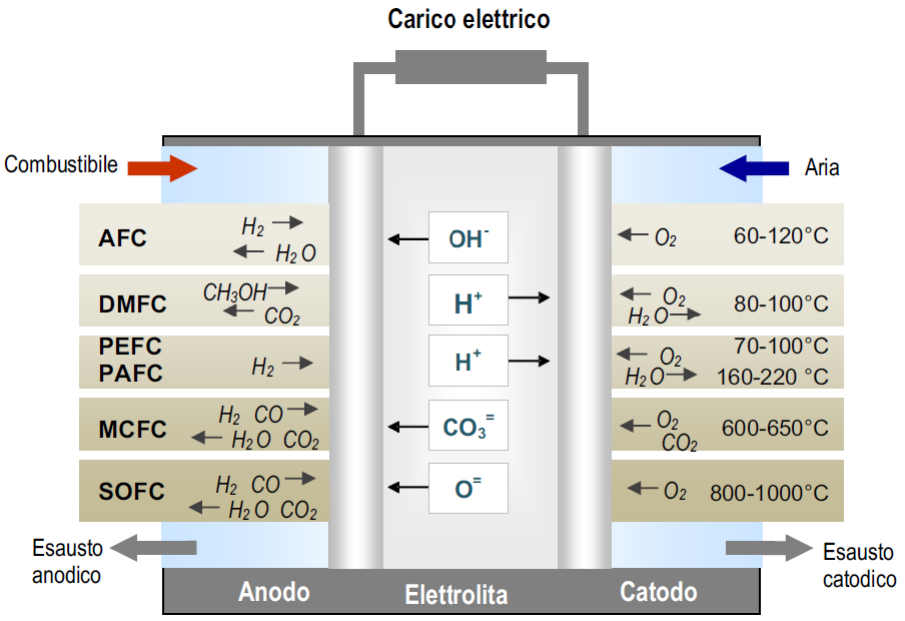

Figure 2.1. Different types of fuel cells

Lastly, **Direct Methanol Fuel Cells (DMFCs)** employ a polymer membrane for the electrolyte and are commonly used in portable applications. Each type of fuel cell offers unique advantages tailored to specific applications, reflecting the ongoing innovation and adaptation in this dynamic field of technology.

2.1.1 Advanced Technologies and Innovations

The future development of this technology aims to improve the efficiency, sustainability and use of hydrogen vehicles by a large number of users. As reported in the paper [21], one of the key aspects of technological progress in fuel cells is the reduction of platinum content in the catalysts. The elevated price of platinum constitutes a significant barrier to the extensive implementation of fuel cells. Recent investigations indicate that low-platinum fuel cell variants have commendable performance, especially regarding efficiency at minimal loads. Nonetheless, these variants demonstrate increased operational instability at elevated power levels relative to conventional fuel cells. To cope with this instability and to achieve the same maximum power output as commercial cells, the number of cells must be increased. Nevertheless, even with an increased number of cells, platinum usage can be reduced by up to 81-97%, resulting in a cost reduction of 27-45%.

Another important area of fuel cell development focuses on optimizing energy management between the battery and the fuel cell. The goal is to maximize efficiency based

on the battery's state of charge (SOC), the system's charging and discharging capabilities, and the minimum power output required from the fuel cell. Additionally, in this context, energy recovery during deceleration (regenerative braking) plays a crucial role, as it improves overall system efficiency by utilizing energy that would otherwise be lost.

One of the major challenges for the development of this technology is the limited availability of hydrogen refueling stations. Investment is needed to expand infrastructure for the production, storage, and distribution of hydrogen.

Another crucial aspect is the production of hydrogen from renewable sources. Currently, most hydrogen is produced using fossil fuels. To improve the sustainability of Fuel Cell Electric Vehicles (FCEVs), it is essential to increase the use of renewable sources in hydrogen production to ensure lower carbon emissions.

2.2 Operating principles

Fuel cells convert the chemical energy of a fuel, typically hydrogen, directly into electrical energy. This process avoids the inefficiencies associated with intermediate thermal cycles, offering superior efficiency compared to conventional internal combustion engines. The fuel cell consists of two electrodes, an anode and a cathode, made from porous materials and separated by an electrolyte. The conversion of chemical energy into electrical energy occurs through oxidation-reduction reactions between hydrogen and oxygen and the conversion takes place on the two electrodes. The electrolyte facilitates the movement of ions produced by one reaction and consumed by the other, thereby completing the electrical circuit within the cell. Additionally, the electrochemical transformation generates heat, which must be dissipated to maintain a constant operating temperature of the cell(Figure 2.2). At the anode, the oxidation reaction occurs where a hydrogen molecule splits into two positive ions, losing two electrons.

$$\mathrm{H_2} \longrightarrow 2\,\mathrm{H^+} + 2\,\mathrm{e^-}$$

The electrons flow through an external circuit, generating an electric current and producing excess heat. The protons move through the electrolyte membrane to the cathode. At the cathode, the electrons and protons combine with oxygen to produce water molecules.

$$\frac{1}{2}\mathrm{O_2} + 2\,\mathrm{H^+} + 2\,\mathrm{e^-} \longrightarrow \mathrm{H_2O}$$

the overall reaction of the system is given by

$$\mathrm{H_2} + \frac{1}{2}\mathrm{O_2} \longrightarrow \mathrm{H_2O}$$

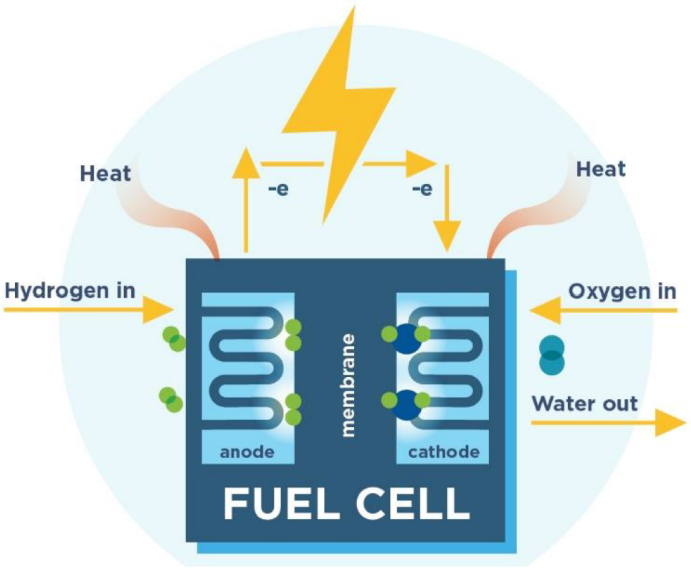

Figure 2.2. Fuel Cell operation

The only waste products are heat, which is released because the reaction is exothermic, and water.

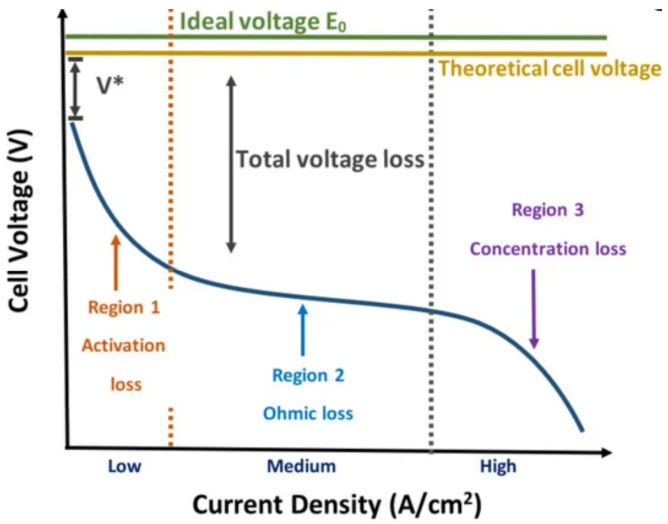

Figure 2.3. Polarization curve

To evaluate fuel cell performance, the polarization curve (Figure 2.3) can be analyzed. It represents the relationship between voltage and current density (A/cm^2), which is the current per unit area. This makes the results scalable, meaning they can be applied

and compared between cells with different surface areas. The manual [15] provides the essential concepts necessary for understanding this curve. The polarization curve presents several key components:

- **Activation Region**: The voltage decreases rapidly as the current increases. These losses are attributed to kinetic reactions and to the activation energy required to start chemical reactions at the electrodes, where reaction rates tend to be relatively low.
- **Ohmic Region**: the main losses are attributed to the internal resistance of the conductors, as described by Ohm's Law $V = R \times I$.
- **Mass Transport Region**: In the final segment of the curve, significant losses occur due to inadequate diffusion of reactants. At this stage, the fuel cell reaches a maximum current density, beyond which it consumes more energy than is provided.
- **Standard potential** E^0: it comes from the formula of Gibbs energy and represents the value for a single reaction (reduction) for a specific electrode. In standard conditions (298 K, 101,325 Pa, all reactans and products are at 1M, Q=1), the maximum energy that it is possible to obtain in a cell, at costant temperature and pressure, is given by the Gibbs free energy:

  $$\Delta G^0 = -nFE^0$$

  From which:

  $$E^0 = -\frac{\Delta G^0}{nF} = 1.229$$

  where:

  - *n= number of electrons participating in the reaction*
  - *F= Farady costant*

The Nerst equation calculates the electrochemical potential, $E = E_{cathode} - E_{anode}$, this is measured under real conditions, in the absence of current, and can be influenced by factors such as concentration, temperature and pressure:

$$E = E^0 - \frac{RT}{nF} lnQ$$

Under standard conditions (where all reactans and products are at 1M, Q=1 e ln(1)=0), the Nerst equation becomes:

$$E = E^0$$

where:

- E^0= *fixed potential for a chemical reaction in standard conditions*
- *T= 298k (25°C)*
- *R = gas constant, 8.314* $\frac{J}{mol \cdot K}$
- ΔG^0 is negative when the cell produces energy (when $E^0 > 0$ and the reaction is spontaneous). It becomes positive when the potential E^0 drops below a certain value (usually 0 V).
- *Q= reaction quotient,* $Q = \frac{[C]^c[D]^d}{[A]^a[B]^b}$, where [C],[D], [A], [B] are the concentrations (or pressures) of the chemical species involved in the reaction and c, d, a, b are the stoichiometric coefficients of the reaction.

The maximum potential difference between the electrodes, E, occurs when no current flows through the external circuit. However, as soon as current starts flowing, the system moves away from equilibrium due to polarization effects. This results in a reduction of the electrical energy supplied compared to the theoretical value, along with an increase in the heat generated.

The analysis of the **efficiency curve** (Figure 2.4) indicates that at low load currents, the electrochemical reaction inside the fuel cell is highly efficient. However, parasitic losses caused by components such as the air compressor and the hydrogen recirculation pump result in a reduction of the system's overall efficiency. As the load current increases, the efficiency initially improves, reaching a peak, but then gradually declines. The decrease in efficiency at higher loads is mainly caused by inefficiencies in the electrochemical process, including activation losses, concentration losses, and increased heat production. Therefore, operating within an optimal load current range is essential for ensuring maximum efficiency in the fuel cell system. [13]

Due to losses, the maximum voltage achievable by each cell is around 1 volt, resulting in reduced power output. However, by combining multiple fuel cells, it is possible to achieve a significant energy output in terms of power, efficiency and flexibility (Figure 2.5).

2.2.1 Architecture

As mentioned in [4], Fuel cell electric vehicles (FCEVs) use electricity to power an electric motor, just like other electric cars. However, FCEVs create electricity using a hydrogen fuel cell instead of only relying on a battery. The vehicle's power is defined based on the

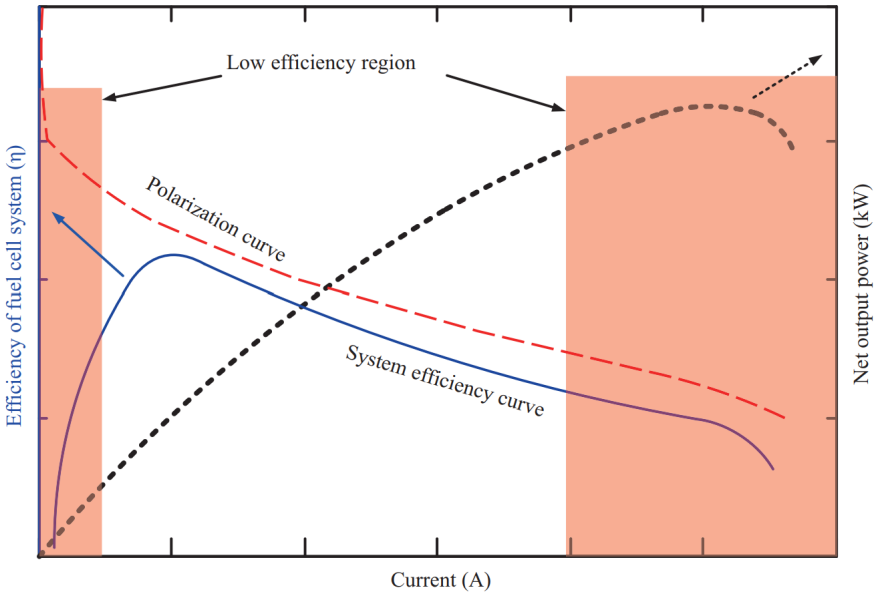

Figure 2.4. Efficiency curve

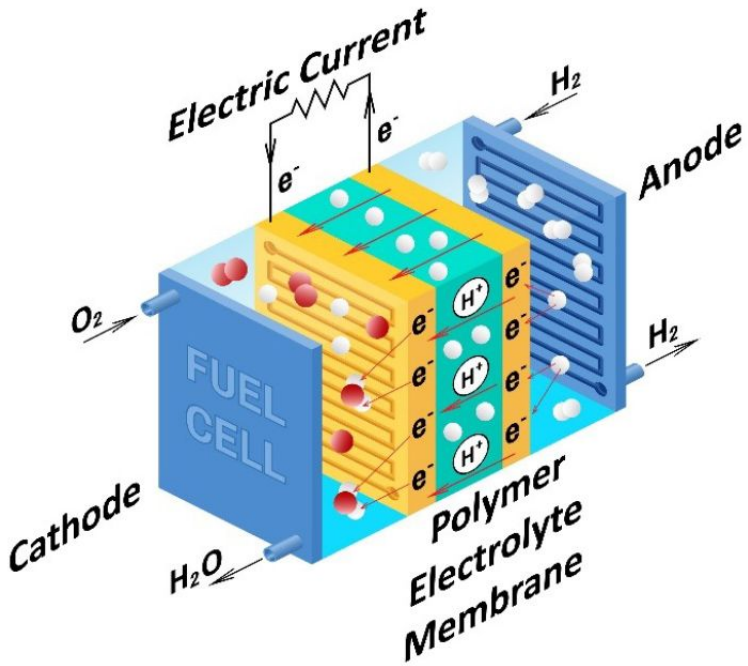

Figure 2.5. Fuel cell stack

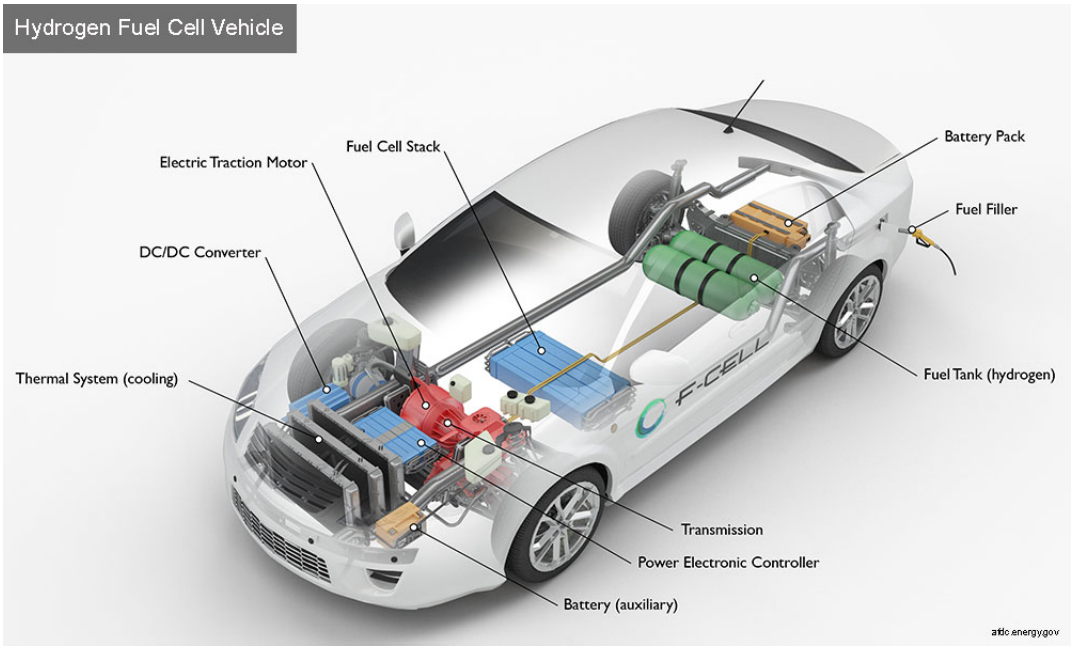

Figure 2.6. Fuel Cell architecture vehicle

electric motor. While FCEVs can be designed to plug in and charge the battery, most of them today use the battery to capture energy from braking, give extra power during quick acceleration, and smooth out the power from the fuel cell. The hydrogen tank size determines how much energy the vehicle can store, unlike all-electric vehicles where the battery size determines both power and energy.

The architecture of FCEVs consists of the integration of many key components, each of which plays a crucial role in order to guarantee optimal performance and safety. In the figure 2.6 the main units are shown.

The heart of the entire system is **the fuel cell stack**. It uses hydrogen and oxigen in order to produce electricity through an electrochemical reaction. This electricity directly powers the electric motor. The fuel cell stack position is generally chosen to guarantee safety and weight balance and depends on the space of the architecture. It is usually placed in the front or center of the vehicle.

The hydrogen tank is another fundamental component. It stores hydrogen gas needed for the proper functioning of fuel cell. It is made by composite material in order to withstand high pressures and ensure safety in case of impact. The tanks are usually located under the vehicle's floor or in the rear. This position should optimize space and protect the tank from potential collisions. The amount of hydrogen the tank can hold determines the vehicle's range which typically varies between 500 and 700 km.

Another essential part is **the auxiliary battery**, that supplies energy for starting the car and powers the vehicle accessories. This battery stores energy recovered from regenerative braking and helps to stabilize the power delivered to the traction system. It is placed near the bottom of the vehicle to keep the center of gravity low and optimize the space.

The electric traction motor drives the vehicle's wheels by taking the electrical energy generated by the fuel cell or stored in the battery and converting it into mechanical energy. The motor can be placed either in the front or in the back, ensuring high performance and decreasing energy losses compared to internal combustion engines.

The high-voltage battery pack stores energy recovered from regenerative braking and supplies extra power to the electric traction motor.

The DC/DC converter transforms the higher-voltage DC power from the traction battery pack into the lower-voltage DC power that is required for vehicle accessories and recharging the auxiliary battery.

The Fuel Filler is a nozzle from the fueling station that connects to the vehicle's inlet to refill the hydrogen storage tank.

The Power Electronics Control regulates the electrical energy flow from the fuel cell and traction battery, controlling the speed and torque of the electric traction motor.

Finally, **thermal system (cooling)** ensures that the operating temperatures for the fuel cell, electric motor, power electronics, and other components are within optimal ranges to avoid overheating. Then, the electric transimission transfers mechanical power from the electric traction motor to the wheels.

2.3 Propulsion Scope in Fuel Cell Vehicles

The fuel cell propulsion module is a system that provides electric power to the vehicle by using the energy produced by a fuel cell along with other powertrain components. This module acts as a gateway and manages the interfaces between the ECU and the fuel cell part. Its primary functions include:

- Power generation through the conversion of the chemical energy from hydrogen and oxygen into electrical energy (power conversion), generating either DC or AC current to power the electric motor.
- Power management, distributing electrical energy to various parts of the vehicle (power distribution), and ensuring optimal performance by coordinating the electric motor with other components (power system integration).

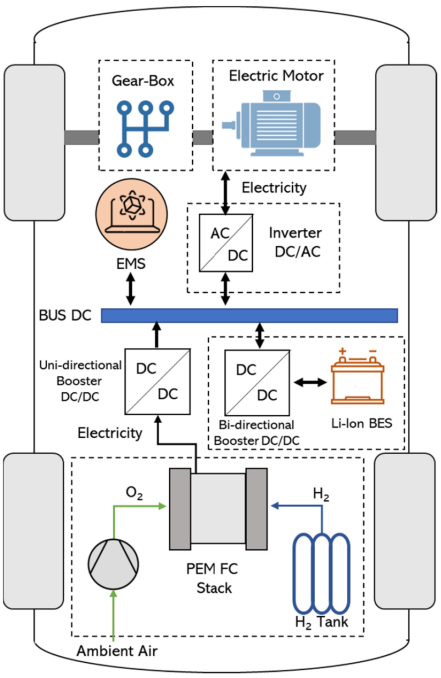

Figure 2.7. Powertrain structure

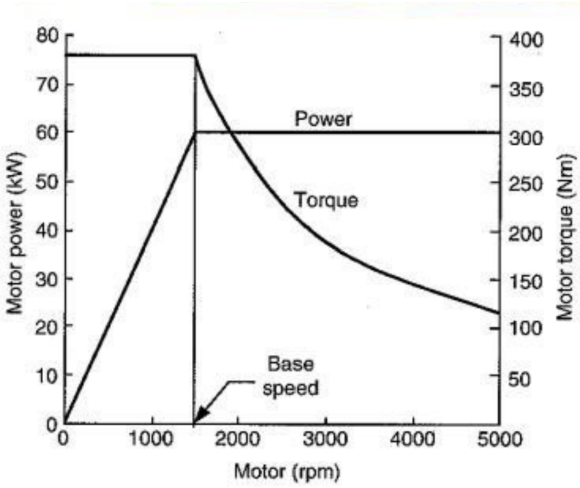

Figure 2.8. Electric Motor Torque/Power Curve

As can be seen in the figure 2.7, the powertrain structure consists of:

- **Fuel cell stack**: It is linked to the DC bus through a unidirectional DC/DC converter, which is essential for managing and regulating the electric power produced by the fuel cell. The converter adjusts the voltage generated by the fuel cell in order

to ensure a constant and stable voltage: the converter is a DC/DC boost converter that connects the output of the fuel cell, boosting its voltage to match the DC bus voltage. Additionally, the fuel cell's role is to supply energy to the system, but it cannot store energy or reverse the power flow. For this reason the FCS generates power that flows in only one direction, towards the motor.

- **Battery**: The battery is connected to the DC bus through a bidirectional DC/DC converter that allows a power flux in both directions: from input to output and viceversa. The converter can either increase or decrease the voltage in both directions. The power flow can be controlled based on the system's operating conditions. The battery has the goal to store energy and it can both supply or absorb power. The bidirectional converter enables the battery to deliver power to the motor when high loads occur, such as during the acceleration, and to absorb power for recharging during regenerative braking.

- **Electric Motor**: The electric motor is powered by the DC bus through a bidirectional DC/AC converter.

- **Operational Method**: The operating strategy involves the battery providing the initial start-up in order to allow to the fuel cell to operate after the low-efficiency zone. During this phase, the battery supplies a large current to power the electric motor. Once the fuel cell is activated, it takes over and sustains the motor's operation [11].

- **Multi-Ratio Transmission System**: The multi-speed transmission plays a crucial role in transferring power from the electric motor to the wheels, allowing the optimization of the vehicle performance and improving overall efficiency. This system adapts the transmission ratio between the wheels and motor based on driving conditions and the power demands.
  By analyzing the power curve (Figure 2.8), which represents the relationship between power and speed, it can be noticed that the motor power increases rapidly at low speeds, reaches a peak related at a certain speed, remains relatively constant over a wide range of speeds. However, when the motor operates at very high speeds, the power may begin to decrease due to mechanical losses ans system inefficiencies. This behaviour is closely linked to the motor's ability to generate torque. At low speeds, the torque is at its maximum and at the same time the power rapidly increases. As speed increases, the torque decreases, resulting in power reaching its maximum before declining. The multi-speed transmission system successfully uses this curve: when high torque is needed, such as during acceleration or start-up, the

system selects a higher gear ratio that allows the motor to operate at lower speed where torque is maximized. Conversely, when the vehicle reaches high speeds and requires less torque, the system shifts to a lower gear ratio, allowing the motor to operate at higher speeds but with a more efficient energy consumption.

Chapter 3

Setup and Configuration of the HIL System

3.1 Overview of the HIL System Setup

The setup is organized into several structured phases to ensure a thorough and systematic approach to testing.

The process begins with defining the Device Under Test (DUT), which specifies the main components of the propulsion system—such as the Fuel Cell Propulsion System (FCPS), Battery Management System (BMS), and Electric Vehicle Management System (EVMS)—that will be integrated into the HIL environment. Following this, the simulation model is developed in Simulink, where the behavior of these components is modeled and prepared for interaction with the simulated vehicle environment.

Next, the wiring harness is created using Napkin software. The wiring harness is a physical interface that connects different control units and components, allowing for proper communication within the system. Using Napkin software to design this harness ensures that all the connections between components, sensors, and actuators are accurately mapped and prepared for the testing environment.

Once the wiring harness is completed, the input/output (I/O) modules are configured through Configuration Desk. This configuration step establishes the communication between the real control units and the simulation model, making sure that the system can send and receive data correctly during testing. Proper I/O configuration is essential for accurate data exchange, as it allows signals to be processed in real-time, simulating actual vehicle behavior.

The setup then moves to executing a sequence of open-loop tests, which test the system's responses without feedback loops, essentially observing how each control unit

behaves independently. Open-loop testing is critical for verifying that each component and system interaction functions correctly before more complex, closed-loop tests are introduced.

One of the final steps in this HIL setup is "flashing", which involves uploading the required software onto each control unit in the system. Flashing ensures that each control unit has the correct software version needed for the simulation, enabling it to respond accurately to the inputs it receives during testing. This step is essential because it synchronizes the software across all components, providing a consistent and reliable testing environment.

In the Hardware-in-the-Loop simulation related to this project, the real nodes are the FCPS (Fuel Cell Propulsion System), BPCM (Battery Pack Control Module), and EVCU (Electric Vehicle Control Unit). Integrating real nodes within the Hardware-in-the-Loop environment offers significant advantages for the testing and validation of automotive systems, particularly when compared to purely simulated nodes.

To implement this flashing process, several steps must be followed:

- Hardware Preparation and Configuration: The control unit is physically connected to the HIL system through communication interfaces (CAN, LIN).
- Software Configuration: Prepare the software that needs to be loaded onto the control unit (usually provided by the supplier).
- Start the Flashing Software and Follow the Instructions.

The integration of a real node offers several advantages over a simulated node, such as:

- Realistic Testing: It allows us to analyze the behavior of the real node in a simulated and controlled environment, providing insights that are more accurate and reflective of actual operating conditions.
- Identifying Hardware and Software Defects: It enables the identification of defects before the system is implemented in a real environment, reducing risks and costs.
- Enhanced Validation: Real nodes allow for the testing of physical characteristics and failure modes that simulations might not accurately replicate.
- Communication Testing: It facilitates testing of the communication between the control unit and other vehicle systems, ensuring that all parts interact correctly in real-world scenarios.
- Closed loop tests.

3.2 Network Topology Analysis

3.2.1 Overview on Network Structure

In today's automotive industry, the layout and the organization of the electronic control units (ECUs) are very important for understanding and defining their interactions and network structure. Network topology, which defines the arrangement of nodes, sensors, actuators and their connections, plays a key role in determining how information flows across the network. It is possible identify two topologies which together constitute the network topology: physical and logical topologies. On one hand, the physical topology deals with the actual layout of the network, the placement and physical connections of the devices and nodes. Common configurations such as star, ring, bus topologies each connect devices differently, conditioning network's performances. On the other hand, logical topology focuses on how data moves through the network. It is crucial for understanding device communication and the operational protocols that facilitate data transmission [5]. In automotive network system [22], star, bus and ring topologies are used to improve the communication between ECUs. The CAN system mostly uses the BUS topology where all units share a single communication channel. This configuration is very effective as it allows each unit to communicate independently: infact, the system resilience is guaranteed even if a node fails.
The ring topology is less common in modern automotive systems and connects each device in a closed loop, providing an alternative path for data if a connection drops.

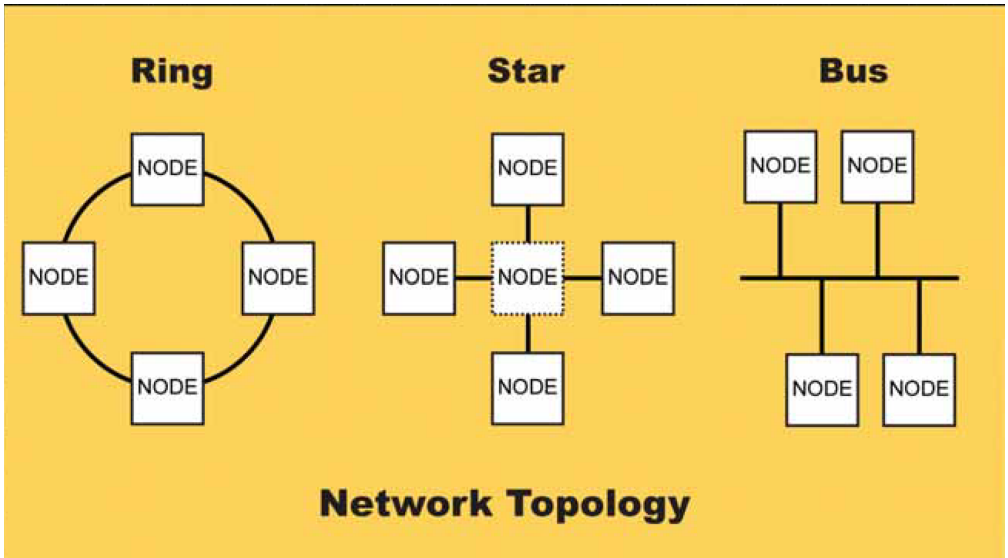

Figure 3.1. Network topologies

The star topology is used for applications that require centralized control: a central node manages the distribution and collection of information from peripheral nodes. This configuration makes the system maintenance and upgrades easier, because adding or removing nodes does not stop the entire network (Figure 3.1). In the network topology

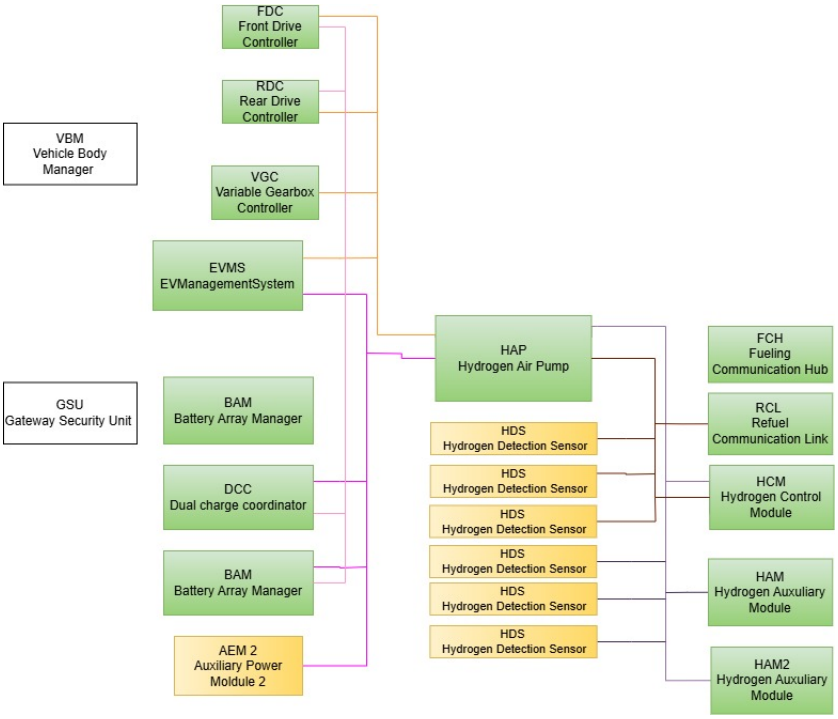

Figure 3.2. Network topology

of the project (Figure 3.2), several functional areas of the vehicle can be identified. The primary ones are:

- Powertrain: This area deals with managing and controlling the motor and transmission. It includes modules such as the Front Drive Controller (FDC) and Rear Drive Controller (RDC). These units respectively manage the control of the front and rear engines and are responsible for the vehicle's propulsion. The Electric Vehicle Management System (EVMS), the Battery Management System (BMS), the Dual Charge Coordinator (DCC), and the Fuel Cell Power System (FCPS) are also integral parts of the powertrain.

- Safety Control: This area includes the Gateway Security Unit (GSU) [2], which ensures the security of the vehicle's communications by blocking suspicious activities in network traffic entering and exiting the vehicle's systems.

- Infotainment: This domain includes modules such as the that handle entertainment functions and vehicle communications, including audio and video systems, navigation, and mobile connectivity. (ETM, TBMM, IPC)
- Chassis: This domain includes systems that support functions such as braking (Brake System Module BSM), suspension, stability control, and steering systems (ASAS), control of the vehicle's transmission (ATC).
- Body: The modules in this area are dedicated to the safety and comfort of passengers and manage various sensors like those related to energy management, helping to prevent battery failures and optimize the vehicle's energy consumption (IBS) [1]. Other modules such as SWSM and CSCW, respectively, monitor the position and movements of the steering wheel and control the cruise control system, which is used to automatically maintain the speed set by the driver. The Vehicle Body Management (VBM) [9] is crucial in this area.

In addition to the main functional areas identified in the vehicle's network topology, it's worth noting that some modules, while primarily linked to one area, also interact with others. This overlap enhances the vehicle's overall functionality.

For example:

- The Electric Vehicle Management System (EVSM), usually part of the powertrain, helps coordinate the engine, chassis, and safety systems to ensure the vehicle runs smoothly and safely.
- The Gateway Security Unit (GSU) not only protects vehicle safety but also secures data communication across the infotainment system.
- Modules like the Battery Management System (BMS) and the Fuel Cell Power System (FCPS) manage the vehicle's power sources but also support body systems by monitoring and optimizing energy use. This contributes to both vehicle safety and energy efficiency.
- The ATC and ASAS, important for the chassis's operation, assist in dynamically adjusting vehicle handling and safety features in response to driving conditions.

This configuration illustrates a contemporary approach to the design of electronic systems in modern vehicles, highlighting the importance of modularity, safety, and efficiency in managing automotive resources. The integration of multiple communication buses and security gateways demonstrates a shift toward increasingly secure and reliable vehicle networks, capable of supporting not only daily functionality but also advanced requirements related to safety and driver assistance systems.

Analyzing the physical topology of the network, it is clear that a bus topology is prevalent in many connections: various devices are connected through a single main communication path. Each device can communicate directly along this bus. This topology is evident in the lines connecting modules such as the BAM, IPC, and SGW. These units are able to communicate over long paths that follow a main line. Furthermore, the bus topology is also used for the FCH (Fueling Communication Hub) and BMS (Battery Management System) modules, due to the need to ensure high reliability. In this case, a fault at one point on the bus could affect communication along the entire segment. Additionally, this type of topology is also identifiable in the powertrain area, specifically for communication connections between the components FDC (Front Drive Controller), RDC (Rear Drive Controller), VGC (Variable Gearbox Controller), and EVMS (Electric Vehicle Management System), which are central in managing propulsion.
The GSU (Gateway Security Unit) and VBM (Vehicle Body Management) appear to act as central hubs, coordinating communications between various modules and serving as a central node to which other nodes connect. In this case, therefore, a star topology is evident. Conversely, there seem to be no ring topologies, which connect nodes in a closed circle. This dual-approach in topology design demonstrates a sophisticated architecture that leverages the strengths of both bus and star configurations. The bus system ensures efficiency and speed in routine operations, while the star configuration offers resilience and enhanced security for critical systems. This design strategy underlines the vehicle's advanced technological framework, capable of supporting both everyday functionality and the higher demands of safety, security, and driver assistance features.

3.2.2 Network Topology - Powertrain

In the network topology related to propulsion, three real nodes can be identified: BMS, FCPS, EVMS. Specifically, BMS controls the vehicle's battery pack, monitoring its charging and discharging, and the health status of the batteries. The Front eBEAM and Rear eBEAM control the front and rear electric motors, respectively, managing traction power and speed adjustments.

The DDC (Dual Charge Coordinator) manages vehicle charging, while the EVMS coordinates vehicle control, ensuring efficient power management between FCPS and other modules.

The FCPS module acts as a gateway, managing the interface between the EVCU and the fuel cell components. It comprises all the hardware elements necessary to generate power through the electrochemical reaction. It is the heart of the propulsion system for a fuel cell vehicle, providing the motive power requires. This module communicates

directly with other simulated nodes such as the HEAC, which controls and compresses the air needed for the reaction in the fuel cells. Sensors monitor pressure, temperature, and hydrogen flow at various parts of the system. In reality, each sensor is strategically positioned in the vehicle to detect specific operational conditions. The RDI manages hydrogen refueling.

The FCCU [3] (Fuel Cell Control Unit) represents the core of the fuel cell system's control: it is responsible for the system's safety, efficiency, and the integration of control functions. It monitors and regulates the propulsion module functions. It has several tasks:

- Gathering data from sensors that measure various physical parameters such as temperature, pressures, and hydrogen flow.
- Analyzing and processing the data to calculate physical quantities necessary for system operations such as energy amounts, power, fuel balance, and compares these values with defined target values.
- Controlling the opening and closing of valves to manage the flow of hydrogen and oxygen, optimizing the chemical reaction. It regulates the temperature by managing the cooling and heating systems to maintain the fuel cell temperature within optimal ranges.
- Detecting anomalies and failures, communicating with the FCPS, which will send a shutdown message or corrective instructions to return the system to optimal operating conditions.

Chapter 4

Hydrogen High-Pressure Tank and Regulator: Modeling and Analysis

This work focused on the development of a Simulink model of the high-pressure system, specifically the hydrogen tank and the pressure regulator located upstream of the fuel cell. The model was implemented in Simulink and used to carry out three different simulation scenarios. It was then integrated in the laboratory into a more complex FCPS (Fuel Cell Power System) model, as part of a Hardware-in-the-Loop (HIL) simulation environment.

To validate the model, real data were collected during a vehicle maneuver lasting approximately thirty minutes. The data analysis was performed offline using CANalyzer, examining the signals transmitted and received by the fuel cell control unit through two separate CAN communication lines. For the analysis, several signals exchanged with the Fuel Cell were examined using a specific vehicle log file.

The case study examined involves the following maneuver, which lasted about 30 minutes: when the vehicle is started, the fuel cell is activated after 80 seconds. For the initial 80 seconds, the fuel cell remains in the 'Off' state. After this period, it transitions into the 'Startup' state, followed by 'Warmup', and then 'Run'. The 'Run' state is maintained even after the vehicle stops but remains powered on. Ultimately, when the vehicle is turned off, the fuel cell enters the 'Shutdown' state. These different operating states of the fuel cell can be observed through the acquired 'mode actual' signal in Figure 4.1 that is transmitted by the FCCU (Fuel Cell Control Unit) and received by the FCPS (Fuel Cell Power System).

Below is a description of the various operating states of the fuel cell and the corresponding numerical values shown in the graph:

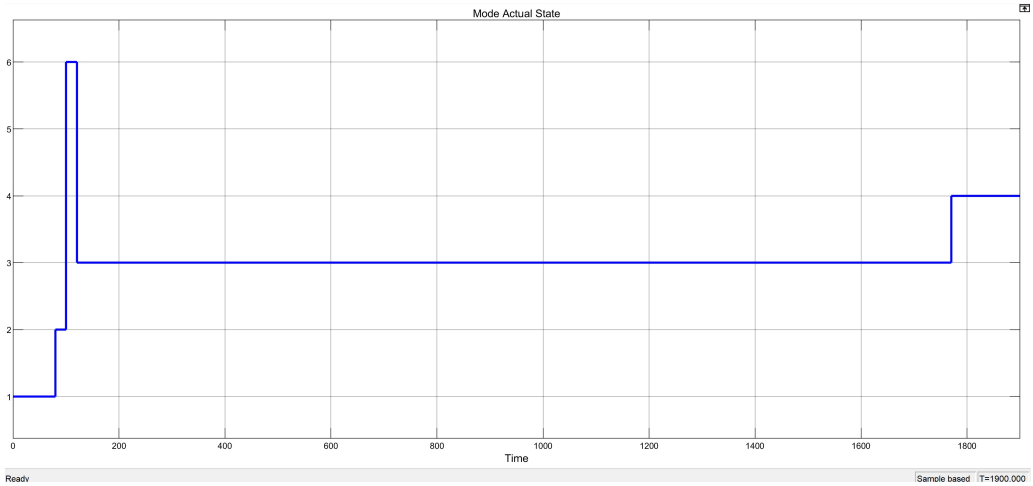

Figure 4.1. Mode Actual State Signal

- Off (1): The fuel cell is completely off and not operating. No hydrogen flow.
- Startup (2): The fuel cell is starting up and preparing for operation. The hydrogen flow begins, and all operational parameters are checked to ensure they are within safe limits.
- Warmup (6): The fuel cell is warming up to reach its optimal operating temperature after a period of inactivity.
- Run (3): The fuel cell is fully operational and supplying power to the system.
- Shutdown (4): The fuel cell is undergoing a controlled shutdown procedure during which all processes are safely terminated.

4.1 Model Description of the Fuel Cell System

The model (Figure 4.2) consists of two main components: the**"HighPressureSystemFC"** and a **Controller**.

The **Controller** receives the "mode actual state" as its input, the signal, in Figure 4.1, transmitted by the Fuel Cell Control Unit (FCCU) and replicated in Simulink through a MATLAB function.

This "mode actual state" input allows the Controller to adjust the valve state, which regulates the flow of hydrogen based on the current system state and the comparison of gas pressure and temperature in the tank against critical maximum values. Within the controller, a state machine (Figure 4.3) has been implemented to determine when the

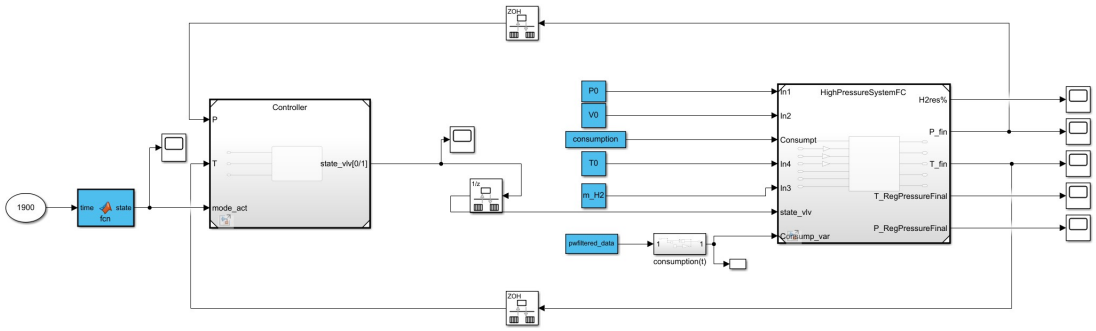

Figure 4.2. Simulink High Pressure Fuel Cell Model

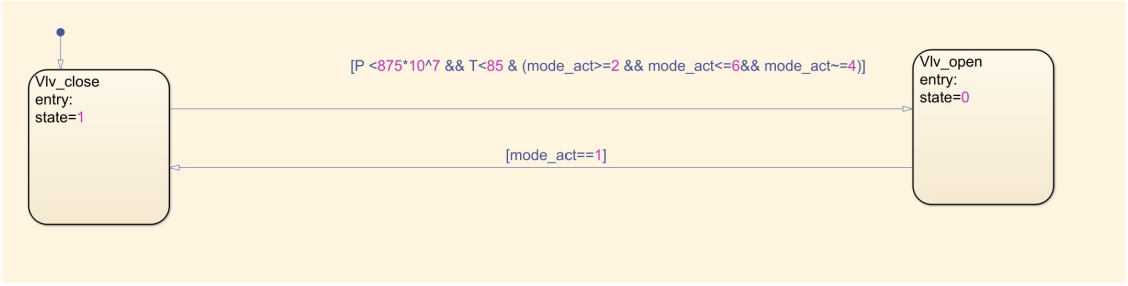

Figure 4.3. Controller: State Machine

signal that enables the valve opening request should be activated or deactivated. Both the `mode_actual` signal and the `state_vlv` signal are generated by Fuel Cell Control Unit (FCCU).

The `mode_actual` signal indicates the current operating state of the fuel cell, while the `state_vlv` signal is computed based on the fuel cell's operating state, as well as on the hydrogen pressure and temperature inside the tank.

If either the pressure or temperature exceeds predefined critical thresholds, the valve remains in the "no request to open" state (`state_vlv = 1`). Otherwise, the signal transitions to the "request to open valve" state (`state_vlv = 0`).

Both signals are transmitted to the Fuel Cell Power System (FCPS), which uses them to manage the physical components accordingly.

The other subsystem, **"HighPressureSystemFC"**, handles the crucial inputs of a high-pressure hydrogen tank as specified by the technical requirements of a fuel cell vehicle. These include managing pressure, temperature, and hydrogen flow, ensuring the

system operates within safe and efficient parameters.

The High Pressure System in the fuel cell vehicle is configured with various critical inputs essential for managing the hydrogen supply and pressure regulation. Below is a detailed description of each input:

1. **P0 (Initial Pressure)**: The system is initialized with a high pressure of 700 bar, which is crucial for maintaining the energy density required for efficient operation.

2. **V0 (Tank Volume)**: The hydrogen tank has a capacity of 160 liters, which ensures adequate hydrogen storage to meet the vehicle's operational requirements over an extended period.

3. **Consumption Formula**: The hydrogen consumption rate is calculated using the formula:
$$\text{Consumption} = \frac{P_{FC}}{\eta \times LHV}$$
where P_{FC} is the constant power demanded by the fuel cell, η denotes the efficiency of the system, and LHV (Lower Heating Value) is the energy released by burning hydrogen.

4. **m_H2 (Hydrogen Mass in the Tank)**: This parameter represents the initial mass of hydrogen in the tank, which is crucial for fuel management and operational planning. The mass is calculated based on the initial conditions within the tank—specifically, the initial gas temperature, the initial pressure, and the molar mass of hydrogen. The Van der Waals equation, which takes into consideration the actual behavior of hydrogen gas, can be used to make more precise estimations under non-ideal situations. First, the Van der Waals equation is used to get the molar volume. The volume of hydrogen in the tank (computed in the chapter later) is then divided by the molar volume to determine the number of moles. The molecular weight of hydrogen is multiplied by this result. Finally, the initial hydrogen mass of 5.6 kg is obtained using this method.

5. **pwfiltered_data (Variable Power Requested from Fuel Cell)**: This input adjusts for variable power demands based on vehicle load and driving conditions, influencing hydrogen flow and system response.

6. **T0 (Ambient Temperature)**: Ambient temperature is considered to account for its impact on hydrogen behavior and fuel cell performance, ensuring system adaptability to environmental conditions.

These inputs guide the system's operational strategies, ensuring efficient and safe management of the fuel cell system's high-pressure components under varying conditions.

This structured approach to system management ensures robust performance and safety, facilitating reliable operations under various conditions.

4.2 Equivalent Hydrogen Tank Model

The real vehicle in the case study is equipped with four high-pressure hydrogen tanks, each holding 40 liters. For simplicity in model development, a single equivalent model with a 160-liter hydrogen tank was chosen. The tank depicted is a Type IV tank (Figure: 4.4), which features a plastic liner designed to prevent hydrogen permeation. This liner is encased in a composite shell made from a polymer matrix reinforced with carbon fibers. This setup enhances the tank's structural integrity while minimizing hydrogen leakage. The liner of a Type IV hydrogen storage tank has the primary function of preventing

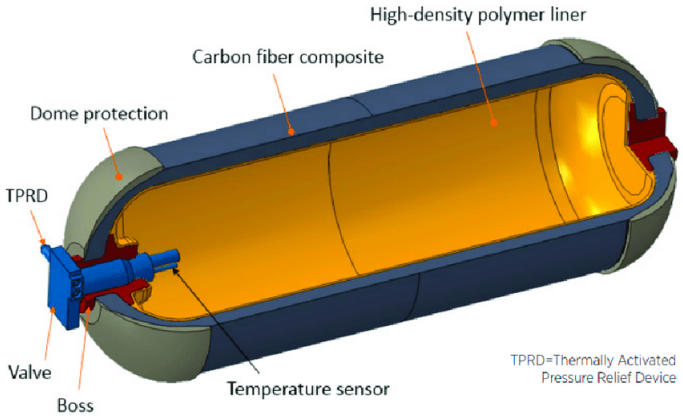

Figure 4.4. Type-IV composite overwrapped hydrogen pressure vessel [10]

hydrogen permeation and ensuring gas containment, while the mechanical resistance to internal pressure is provided by the carbon fiber-reinforced polymer (CFRP) wrap.

Hydrogen permeation refers to the process by which hydrogen molecules diffuse through a solid material, potentially leading to gas loss and reduced system efficiency. The mechanical resistance to internal pressure, on the other hand, is the ability of the CFRP structure to withstand the high stresses generated by compressed hydrogen at 700 bar, preventing structural deformation or failure.

Studies conducted by Miyake et al. (2018) and Zhao et al. (2020) on Type IV tanks at 700 bar report liner thickness values between 6 mm and 8 mm, with thermomechanical simulation models adopting an average value of 7 mm to ensure a sufficient barrier to

hydrogen permeation and adequate structural stability [23].

Furthermore, a cost analysis conducted by NREL (2020) suggests that liner thickness significantly affects the overall weight of the tank, with design optimizations balancing the need to reduce system mass while maintaining high performance [19].

Based on these references, a 7 mm liner thickness was adopted for the model analyzed in this study, aligning with the technical specifications of Type IV tanks used in fuel cell vehicles (FCEVs). Based on industrial standards and geometric constraints, the equivalent tank is assumed to be **cylindrical**, with an **internal diameter** of 0.412 m and a **length** of 1.2 m. The tank consists of:

- A **liner PA6/PA12** with a thickness of 7 mm.
- An **outer shell** composed of **carbon fiber-reinforced polymer (CFRP)**, with a thickness of 15 mm.

To verify that the selected dimensions provide the correct internal volume, we use the formula for the volume of a cylinder:

$$V_{\text{int}} = \pi \left(\frac{d_{\text{int}}}{2} \right)^2 \times L \tag{4.1}$$

Substituting the values:

$$V_{\text{int}} = \pi \left(\frac{0.412}{2} \right)^2 \times 1.2 \tag{4.2}$$

$$V_{\text{int}} \approx 0.159\,97\,\text{m}^3 \approx 160\,\text{l} \tag{4.3}$$

This confirms that the selected dimensions are consistent with the required storage capacity.

4.3 Mass and Thermal Properties Assessment

4.3.1 Calculation of Gaseous Hydrogen Mass Using Van der Waals Equation

Since hydrogen is stored at very high pressures, the ideal gas law is not sufficiently accurate to determine its mass. Instead, the Van der Waals equation of state is used:

$$\left(P + \frac{an^2}{V^2} \right) (V - nb) = nRT \tag{4.4}$$

where:

- P is the pressure (Pa),
- V is the total volume of the hydrogen gas inside the tank (m^3),
- n is the number of moles of hydrogen in the tank,
- R is the universal gas constant ($R = 8.314$ J/(mol · K)),
- T is the absolute temperature (K),
- a and b are Van der Waals constants for hydrogen:

$$a = 0.0244\,\text{Pa} \cdot \text{m}^6/\text{mol}^2$$
$$b = 2.65 \times 10^{-5}\,\text{m}^3/\text{mol}$$

Rearranging for n, we obtain the following nonlinear equation:

$$P(V - nb) + \frac{an^2}{V^2} = nRT \tag{4.5}$$

which can be solved numerically to find n. Once n is determined, the total mass of gaseous hydrogen is given by:

$$m_{\text{H}_2} = nM_{\text{H}_2} \tag{4.6}$$

where:

- $M_{\text{H}_2} = 2.016$ g/mol is the molar mass of hydrogen.

4.3.2 Determination of the Liner Mass

The hydrogen tank considered in this study has a capacity of 160 liters and operates at a pressure of 700 bar. For its geometry, a cylindrical shape is assumed with a length-to-diameter ratio of $L/D \approx 3$, in accordance with typical specifications of high-pressure hydrogen tanks used in fuel cell vehicles [6, 19].

Based on this ratio and considering the tank volume, the estimated diameter is approximately 0.412 m, and the length is approximately 1.2 m, calculated using the volume equation for a cylinder:

$$V = \pi \left(\frac{D}{2}\right)^2 L \tag{4.7}$$

By assuming $L/D = 3$, the length can be expressed as:

$$L = 3D \tag{4.8}$$

Substituting into the first equation and solving for D:

$$D = \left(\frac{4V}{\pi L/D}\right)^{1/3} \tag{4.9}$$

From which the final values are obtained:

$$D \approx 0.412 \text{ m}, \quad L \approx 1.2 \text{ m} \tag{4.10}$$

These values align with tanks used in the Toyota Mirai and Hyundai Nexo, which adopt a design with L/D between 3 and 3.5 to optimize space utilization and ensure adequate structural resistance [6, 19].

The mass of the liner can be determined using the **density** of the material and its **volume**:

$$m_{\text{liner}} = V_{\text{liner}} \cdot \rho_{\text{liner}} \tag{4.11}$$

where:

- m_{liner} is the mass of the liner (kg),
- V_{liner} is the **volume of the liner** (m^3),
- ρ_{liner} is the **density of the liner material** (kg/m^3).

4.3.3 Volume Calculation of the Liner

The **volume of the liner** is calculated based on the **total internal surface area of the tank** and the **liner thickness**:

$$V_{\text{liner}} = A_{\text{liner}} \cdot s_{\text{liner}} \tag{4.12}$$

where:

- A_{liner} is the total **internal surface area** of the tank,
- s_{liner} is the **liner thickness**.

Assuming a **cylindrical tank** with an **internal diameter of** 0.412 m and **length of** 1.2 m, the internal surface area is:

$$A_{\text{liner}} = 2\pi rL + 2\pi r^2 \tag{4.13}$$

$$A_{\text{liner}} = 2\pi \times \left(\frac{0.412}{2}\right) \times 1.2 + 2\pi \times \left(\frac{0.412}{2}\right)^2 \tag{4.14}$$

$$A_{\text{liner}} \approx 1.82\,\text{m}^2 \tag{4.15}$$

Given a **liner thickness of** 7 mm (0.007 m), the volume of the liner is:

$$V_{\text{liner}} = 1.82 \times 0.007 = 0.012\,74\,\text{m}^3 \tag{4.16}$$

4.3.4 Calculation of the CFRP Shell Mass

The mass of the Carbon Fiber Reinforced Polymer (CFRP) shell is calculated based on the known geometric parameters of the hydrogen storage tank. The CFRP shell mass is determined by the volume difference between the external and internal cylinder, multiplied by the CFRP density:

$$m_{\text{CFRP}} = V_{\text{CFRP}} \cdot \rho_{\text{CFRP}} \tag{4.17}$$

where:

- V_{CFRP} is the volume of the CFRP shell, calculated as the difference between the external and internal cylinder volumes.
- $\rho_{\text{CFRP}} = 1600$ kg/m^3 is the typical density of CFRP.

The volume of the CFRP shell is given by:

$$V_{\text{CFRP}} = \frac{\pi}{4} L \left(D_{\text{ext}}^2 - D_{\text{int}}^2\right) \tag{4.18}$$

where:

- $D_{\text{int}} = 0.412$ m is the internal diameter of the tank.
- $D_{\text{ext}} = D_{\text{int}} + 2s_{\text{CFRP}} = 0.456$ m is the external diameter of the tank.
- $s_{\text{CFRP}} = 22$ mm (0.022 m). It consists of the CFRP shell, which is 15 mm, plus the liner thickness.
- $L = 1.2$ m is the length of the tank.

Substituting the values:

$$V_{\text{CFRP}} = \frac{\pi}{4} \times 1.2 \times (0.456^2 - 0.412^2) \tag{4.19}$$

$$= 0.0359 \text{ m}^3 \tag{4.20}$$

Now, calculating the mass:

$$m_{\text{CFRP}} = V_{\text{CFRP}} \times \rho_{\text{CFRP}} \tag{4.21}$$

$$m_{\text{CFRP}} = 0.0296 \times 1600 = 57.59 \text{ kg} \tag{4.22}$$

Thus, the total mass of the CFRP shell is $m_{\text{CFRP}} = 57.59$ kg for a hydrogen tank with an internal diameter of 0.412 m, a CFRP shell thickness of 15 mm, and a length of 1.2 m.

Table 4.1. Summary of CFRP Shell and Liner Masses with Tank Dimensions

Parameter	**Value**	**Units**
Tank Volume	160	liters
Tank Internal Diameter	0.412	meters
Tank Length	1.2	meters
Liner Thickness	7	mm
Liner Surface Area	1.8	square meters
Liner Volume	0.01274	cubic meters
Liner Mass (PA6/PA12)	10.87	kg
CFRP Shell Volume	0.0359	cubic meters
CFRP Shell Mass	57.59	kg

4.4 Initial Condition

4.4.1 Assumption: Initial Hydrogen Temperature Estimation

In this section, a hypothetical scenario is considered, in which the hydrogen refueling has just been completed before the start of the driving operation. The initial temperature of the hydrogen inside the tank is assumed to be 318.345 K. This assumption is justified based on typical operating conditions for a fuel cell vehicle immediately after refueling at an H70 station. During refueling, hydrogen is compressed to 700 bar and pre-cooled

to -40°C, as prescribed by SAE J2601. However, the compression process itself leads to a significant temperature rise. Under real-world operating conditions, the gas temperature after filling typically ranges between 320 K and 350 K [14], depending on ambient temperature, the efficiency of the pre-cooling system, and the refueling duration.

The gaseous hydrogen then begins to exchange heat with the internal liner of the tank, whose initial temperature is influenced by the external ambient temperature. Assuming a temperate climate with an ambient temperature of approximately 30°C, the initial temperature of the liner is taken as 308 K.

4.4.2 Thermal Equilibrium Calculation

When hydrogen is stored at 700 bar, its temperature after refueling is elevated due to the compression process. However, thermal interaction with the tank liner, initially at a lower temperature, leads both components—gas and liner—to an equilibrium temperature T_{eq}.

Assuming no heat exchange with the external environment in the short term, the system can be considered thermally isolated. By applying the principle of energy conservation:

$$Q_{\text{lost by gas}} + Q_{\text{gained by liner}} = 0 \tag{4.23}$$

where Q represents heat exchanged. The gas releases heat ($Q < 0$), while the liner absorbs heat ($Q > 0$). Using the definition of thermal energy $Q = C\Delta T$, the thermal balance equation becomes:

$$C_{\text{H}_2}(T_{\text{eq}} - T_{\text{H}_2,\text{initial}}) + C_{\text{liner}}(T_{\text{eq}} - T_{\text{liner, initial}}) = 0 \tag{4.24}$$

where:

- $C_{\text{H}_2} = m_{\text{H}_2} c_v$ is the total thermal capacity of hydrogen,
- $C_{\text{liner}} = m_{\text{liner}} c_p$ is the total thermal capacity of the liner,
- $T_{\text{H}_2,\text{initial}}$ is the initial hydrogen temperature after refueling,
- $T_{\text{liner, initial}}$ is the initial temperature of the liner.

Rearranging for T_{eq}:

$$T_{\text{eq}} = \frac{C_{\text{H}_2} T_{\text{H}_2,\text{initial}} + C_{\text{liner}} T_{\text{liner, initial}}}{C_{\text{H}_2} + C_{\text{liner}}} \tag{4.25}$$

This equation shows that T_{eq} is a weighted average of the initial temperatures, proportional to the thermal capacities:

- If $C_{H_2} \gg C_{\text{liner}}$, T_{eq} is closer to the hydrogen temperature.
- If $C_{\text{liner}} \gg C_{H_2}$, T_{eq} is closer to the liner temperature.

4.4.3 Initial Temperature of the Liner

Before vehicle operation, the liner temperature is assumed to be 300 K, reflecting equilibrium with the ambient environment. Studies on high-pressure hydrogen storage [12] confirm that the liner remains near ambient temperature before refueling. Due to the rapid refueling process (lasting only a few minutes), the liner does not reach thermal equilibrium with the hydrogen, which initially enters at 330 K-350 K due to compression heating.

Experimental results on Type IV hydrogen tanks confirm that immediately after refueling, the liner temperature remains below the hydrogen temperature for a certain period. Based on these observations, an initial liner temperature of 308 K is assumed.

4.4.4 Thermal Balance Including the CFRP Shell

Expanding the thermal balance to include the CFRP shell, the equilibrium temperature equation becomes:

$$T_{\text{eq}} = \frac{C_{H_2} T_{H_2,\text{initial}} + C_{\text{liner}} T_{\text{liner, initial}} + C_{\text{CFRP}} T_{\text{CFRP, initial}}}{C_{H_2} + C_{\text{liner}} + C_{\text{CFRP}}} \tag{4.26}$$

where:

- $C_{\text{CFRP}} = m_{\text{CFRP}} c_p$ is the thermal capacity of the CFRP shell.

To calculate the thermal equilibrium temperature, we first need to introduce the equivalent model of the tank, including the mass of the liner, the shell, and the hydrogen.

Tank Specifications

4.4.5 Numerical Calculation of T_{eq}

Using the following thermal capacities:

$$C_{H_2} = m_{H_2} c_v = (5.6 \text{ kg})(10.184 \text{ kJ/kgK}) = 57.03 \text{ kJ/K} \tag{4.27}$$

$$C_{\text{liner}} = m_{\text{liner}} c_p = (10.87 \text{ kg})(1.8 \text{ kJ/kgK}) = 19.57 \text{ kJ/K} \tag{4.28}$$

$$C_{\text{CFRP}} = m_{\text{CFRP}} c_p = (57.59 \text{ kg})(1 \text{ kJ/kgK}) = 57.59 \text{ kJ/K} \tag{4.29}$$

Table 4.2. Equivalent Hydrogen Tank Specifications

Parameter	**Value**
Total internal volume	160 L
Internal diameter	0.412 m
Length	1.2 m
Liner material	PA6/PA12
Liner thickness	7 mm
Outer shell material	CFRP
Outer shell thickness	15 mm

Assuming initial temperatures:

$$T_{\mathrm{H_2,initial}} = 330\,\mathrm{K} \tag{4.30}$$

$$T_{\text{liner, initial}} = 308\,\mathrm{K} \tag{4.31}$$

$$T_{\text{CFRP, initial}} = 308\,\mathrm{K} \tag{4.32}$$

Substituting in Eq. (4.26):

$$T_{\mathrm{eq}} = \frac{(57.03 \times 330) + (19.57 \times 308) + (57.59 \times 308)}{57.03 + 19.57 + 57.59} \approx 317.35\ \mathrm{K} \tag{4.33}$$

Thus, the initial temperature of hydrogen in the simulation is set to 317 K, aligning with literature and experimental data for Type IV hydrogen tanks in FCEVs operating in temperate climates.

4.4.6 Thermal Balance of the Hydrogen Tank

Assuming that the gas and the internal wall of the tank are in thermal equilibrium, the energy balance can be simplified to a single equation. The heat transfer from the hydrogen gas to the ambient occurs through three mechanisms:

1. Convection between the hydrogen gas and the internal tank wall, characterized by the heat transfer coefficient h_{gas}.

2. Conduction through the tank wall, which consists of two layers:

   - The internal liner, with thermal conductivity k_{liner} and thickness d_{liner}.
   - The external composite shell (CFRP), with thermal conductivity k_{CFRP} and thickness d_{CFRP}.

3. Convection between the external tank wall and the surrounding air, with heat transfer coefficient h_{ext}.

Since these heat transfer mechanisms act in series, the overall effective heat transfer coefficient h_{eff} is given by:

$$\frac{1}{h_{\text{eff}}} = \frac{1}{h_{\text{gas}}} + \frac{d_{\text{liner}}}{k_{\text{liner}}} + \frac{d_{\text{CFRP}}}{k_{\text{CFRP}}} + \frac{1}{h_{\text{ext}}} \tag{4.34}$$

where:

- h_{gas} is the convective heat transfer coefficient between the hydrogen and the internal wall (W/m²K),
- k_{liner} and k_{CFRP} are the thermal conductivities of the liner and the composite shell, respectively (W/mK),
- d_{liner} and d_{CFRP} are the thicknesses of the liner and the composite shell (m),
- h_{ext} is the convective heat transfer coefficient between the external wall and the ambient air (W/m²K),
- h_{eff} is the overall effective heat transfer coefficient (W/m²K).

Using h_{eff}, the total heat transfer rate between the hydrogen and the environment is:

$$\dot{Q} = h_{\text{eff}} A_{\text{wall}} (T_{\text{amb}} - T) \tag{4.35}$$

where:

- A_{wall} is the tank surface area (m²),
- T_{amb} is the ambient temperature (K),
- T is the common temperature of both the gas and the internal wall (K).

4.4.7 Choice of the Simplified Model

Since the gas and the internal tank wall are assumed to be in thermal equilibrium, the energy exchange inside the tank is considered instantaneous. This assumption allows for a simplification of the effective heat transfer coefficient by neglecting the internal convective resistance $1/h_{\text{gas}}$. Thus, the simplified form of h_{eff} is given by:

$$\frac{1}{h_{\text{eff}}} = \frac{d_{\text{liner}}}{k_{\text{liner}}} + \frac{d_{\text{CFRP}}}{k_{\text{CFRP}}} + \frac{1}{h_{\text{ext}}} \tag{4.36}$$

This simplification is valid under the assumption that the heat transfer between the hydrogen and the tank wall occurs much faster than the heat transfer from the tank to the environment. By using this reduced model, the computational complexity is significantly decreased while still providing an accurate representation of the thermal dynamics of the system.

To simplify the equation, we can combine the thermal resistances of the liner and CFRP into a single equivalent resistance. This step assumes that the combined effect of these materials can be represented by average values of their thickness and thermal conductivity:

$$\frac{d}{k} = \frac{d_{\text{liner}}}{k_{\text{liner}}} + \frac{d_{\text{CFRP}}}{k_{\text{CFRP}}} \tag{4.37}$$

Thus, substituting the combined thermal resistance back into the original equation gives us:

$$\frac{1}{h_{\text{eff}}} = \frac{d}{k} + \frac{1}{h_{\text{ext}}} \tag{4.38}$$

This simplified equation still retains the external convective resistance term, which is crucial for understanding the overall thermal behavior but reduces complexity by merging the conductive resistances into a single term. Using h_{eff}, the total heat transfer rate between the hydrogen and the environment is:

$$\dot{Q} = h_{\text{eff}} A_{\text{wall}} (T_{\text{amb}} - T) \tag{4.39}$$

where:

- A_{wall} is the tank surface area (m^2),
- T_{amb} is the ambient temperature (K),
- T is the common temperature of both the gas and the internal wall (K).

4.5 Final Energy Balance Equation

The energy balance for the system, considering the internal equilibrium assumption, is given by:

$$(m_{\text{H}_2} c_v + m_{\text{wall}} c_{p,\text{wall}}) \frac{dT}{dt} = h_{\text{eff}} A_{\text{wall}} (T_{\text{amb}} - T) - \dot{m}_{\text{H}_2} h_{\text{out}} \tag{4.40}$$

where:

- $m_{\mathrm{H_2}}$ is the mass of hydrogen inside the tank (kg),
- c_v is the specific heat capacity of hydrogen at constant volume (J/kgK),
- m_{wall} is the mass of the tank wall (kg),
- $c_{p,\mathrm{wall}}$ is the specific heat capacity of the tank material (J/kgK),
- $\dot{m}_{\mathrm{H_2}}$ is the mass flow rate of hydrogen leaving the tank (kg/s),
- h_{out} is the specific enthalpy of the exiting hydrogen (J/kg).

This equation represents the thermal evolution of the hydrogen inside the tank, taking into account heat losses to the environment and the cooling effect due to hydrogen consumption.

4.6 Consideration of Mass Flow Energy Loss in the Thermal Balance

In the thermal balance equation of the hydrogen tank, the term related to the energy loss due to the mass flow of hydrogen leaving the tank is given by:

$$\dot{Q}_{\mathrm{out}} = \dot{m}_{\mathrm{H_2}} c_p T \tag{4.41}$$

where:

- $\dot{m}_{\mathrm{H_2}}$ is the mass flow rate of hydrogen leaving the tank (kg/s),
- c_p is the specific heat capacity of hydrogen at constant pressure (J/kgK),
- T is the temperature of the hydrogen inside the tank (K).

This term represents the thermal energy carried away by the hydrogen that exits the tank. Its inclusion in the thermal balance equation depends on the significance of the hydrogen mass flow rate compared to the total mass of hydrogen inside the tank.

4.6.1 When Should This Term Be Included?

The term $\dot{m}_{\mathrm{H_2}} c_p T$ should be considered in the thermal balance when:

- The mass flow rate of hydrogen is significant compared to the total hydrogen mass, leading to non-negligible energy loss.
- The hydrogen expansion causes noticeable cooling due to the Joule-Thomson effect.

- The hydrogen tank is relatively small, making the energy extracted by the mass flow more impactful on the internal temperature.

In these cases, neglecting this term could lead to an overestimation of the internal temperature of the hydrogen.

4.6.2 When Can This Term Be Neglected?

On the other hand, this term can be neglected in the thermal balance if:

- The variation of hydrogen mass inside the tank is very small over time, meaning $m_{\mathrm{H_2}}$ remains nearly constant.
- The hydrogen exits gradually and does not cause rapid cooling.
- The energy loss due to mass flow is minor compared to the heat exchanged with the environment via conduction and convection.

If this term is considered negligible, the thermal balance equation simplifies to:

$$(m_{\mathrm{H_2}} c_v + m_{\mathrm{wall}} c_{p,\mathrm{wall}}) \frac{dT}{dt} = h_{\mathrm{eff}} A_{\mathrm{wall}} (T_{\mathrm{amb}} - T) \tag{4.42}$$

where the temperature evolution is driven only by the heat exchange with the external environment.

Chapter 5

Evaluation of Three Diagnosis Approaches in the Model

5.1 Real Scenario

In the real study scenario, the initial temperature of the hydrogen inside the tank is assumed to be equal to the ambient temperature. This hypothesis is justified by considering a state of thermal equilibrium between the gas, the tank walls, and the external environment at the initial time.

This means that no initial heat exchange is expected within the system, as all components share the same temperature. Nevertheless, as the system evolves, temperature changes occur due to heat transfer with the environment and hydrogen outflow.

The thermal behavior of the gas is governed by the following energy balance equation (equation 4.40):

$$(m_{\mathrm{H_2}} c_v + m_{\mathrm{wall}} c_{p,\mathrm{wall}}) \frac{dT}{dt} = h_{\mathrm{eff}} A_{\mathrm{wall}} (T_{\mathrm{amb}} - T) - \dot{m}_{\mathrm{H_2}} h_{\mathrm{out}} \tag{5.1}$$

The model includes three different simulation scenarios, each defined by specific input conditions applied to the `High Pressure System FC` submodel. Each simulation can be executed by changing the variant condition set in the Simulink workspace, allowing the activation of the corresponding configuration within the model.

For example, within the `High Pressure System FC` block, the diagram below shows the structure of the `Variant Subsystem` (Figure 5.1). In this case, the variant condition activates the first simulation. The inputs highlighted in normal font correspond to the signals used in this specific simulation scenario, while the faded (grayed-out) inputs belong to the other two simulation variants and are therefore inactive in this configuration. Each

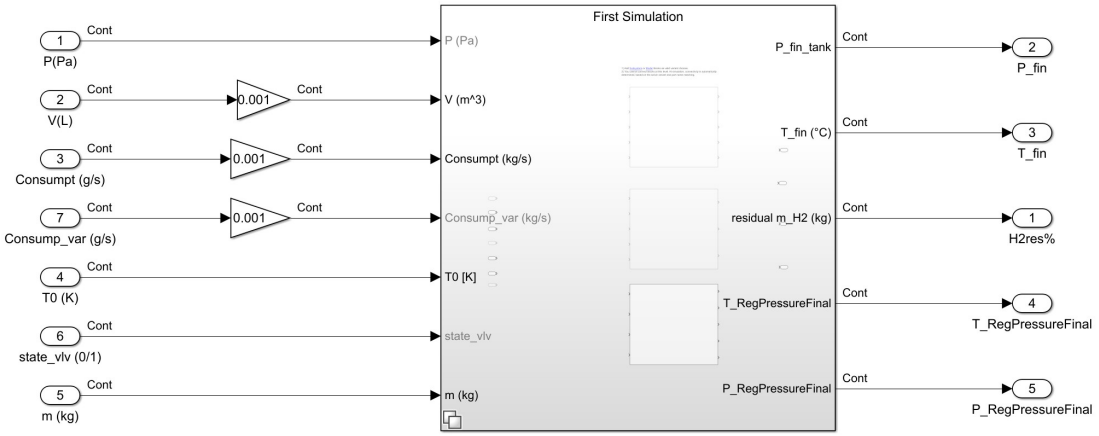

Figure 5.1. Variant Subsystem block showing the active configuration for the first simulation.

variant introduces specific differences in the modeling assumptions and input signals:

- **First Simulation:** This case considers only the thermal balance within the tank. The energy exchange is modeled using the heat balance equation 5.1.
- **Second Simulation:** In addition to the thermal balance, this case also takes into account the valve state. The valve opening or closing (represented by the signal `state_vlv`) directly influences whether hydrogen is allowed to flow out of the tank, thereby affecting the mass and pressure evolution.
- **Third Simulation:** This variant extends the previous case by introducing a dynamic convection coefficient that varies depending on the vehicle's status (moving or stationary). Convective heat transfer is much less while the car is stationary but still running on. Moreover, the fuel cell power requirement is seen as variable rather than constant; so, hydrogen consumption is computed as a time-dependent function using a variable power input.

5.1.1 Differences Between the Three Simulation Models

The core structure for calculating the temperature and pressure inside the hydrogen tank, as well as at the outlet of the pressure regulator, remains the same for all three simulation models and is shown in Figure 5.2 (core architecture for the first simulation, with constant hydrogen consumption). In this first simulation, only a constant hydrogen consumption

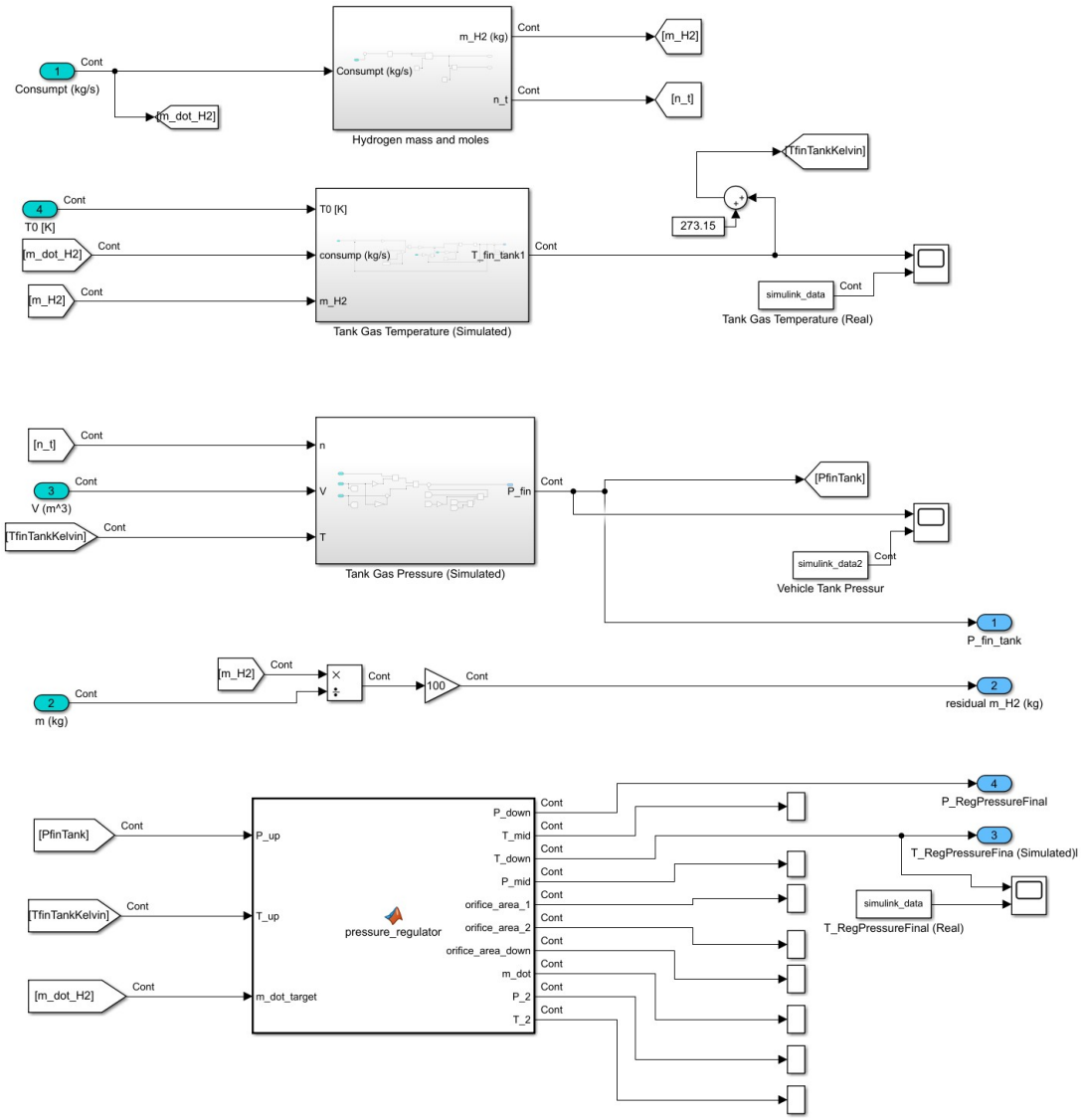

Figure 5.2. Core structure for calculating the outputs model

is considered as input. Neither the valve state signal (`state_vlv`) nor the vehicle speed are included in the model.

This architecture includes the computation of hydrogen mass and moles, tank gas temperature, tank pressure using the ideal gas law, residual hydrogen mass, and the thermodynamic modeling of the pressure regulator.

What differentiates the three simulation scenarios are the input conditions:

- the hydrogen mass flow rate (constant or variable),

- the valve state signal (`state_vlv`),
- and the vehicle motion status, which affects the convection coefficient used in the thermal balance.

These inputs influence how the core model behaves under different operating conditions, without changing the internal structure of the simulation blocks.

5.1.2 Core Modeling Structure – First Simulation

The core of the first simulation is composed of several interconnected subsystems that calculate key physical quantities related to the hydrogen tank and the pressure regulation process. The main blocks are described below:

- **Hydrogen Mass and Moles**: This block calculates the instantaneous hydrogen mass m_{H_2} and number of moles n_{H_2} inside the tank based on the input hydrogen consumption rate. The molar mass of hydrogen is used to convert the mass flow rate from kg/s to mol/s.

  This block forms the basis for subsequent thermodynamic calculations, such as pressure and temperature inside the tank, which depend directly on the evolving hydrogen mass and moles.

- **Tank Gas Temperature (Simulated)**: This block implements the thermal model of the hydrogen in the tank. It solves the energy balance equation assuming a closed system. The resulting temperature T_{fin} is compared to real data (if available) to validate the model.

- **Tank Gas Pressure (Simulated)**: The Van der Waals equation is used instead of the ideal gas law to calculate the Pressure inside the tank. The gas pressure inside the tank is computed from the current moles, temperature, and volume. The output pressure is compared to real vehicle tank pressure for validation.

- **Residual Hydrogen Mass**: This block computes the remaining hydrogen mass in the tank by subtracting the consumed amount from the initial mass.

- **Pressure Regulator Model (`regolatore_pressione`)**: This subsystem simulates the thermodynamic behavior across the pressure regulator. Given the upstream pressure and temperature, and the mass flow rate, the model calculates the downstream pressure $P_{\text{RegPressureFinal}}$ and temperature $T_{\text{RegPressureFinal}}$, taking into account thermodynamic expansion and heat exchange. The regulator model

also includes intermediate values such as T_{mid}, A_{orifizio}, and flow dynamics used for internal analysis.

This structure allows for a physically consistent simulation of the tank's dynamic response and provides a baseline for comparing more complex cases, such as those including valve state or vehicle speed effects.

5.2 Hydrogen Mass and Moles Calculation

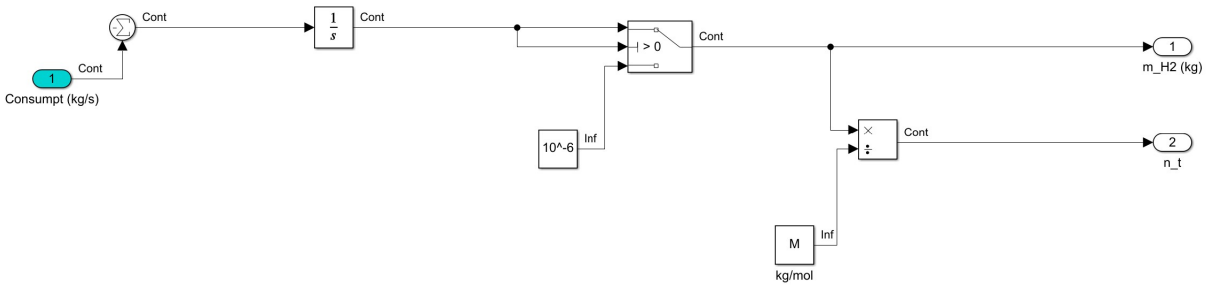

Figure 5.3. Hydrogen Mass and Moles Calculation

The first block in the model calculates the total mass and the number of moles of hydrogen available in the tank over time, based on the hydrogen consumption rate (Figure 5.3).

Input: Hydrogen Consumption

The block receives as input the hydrogen mass flow rate $\dot{m}_{\text{H}_2}$ in kg/s, denoted as `Consumpt`. The hydrogen consumption rate is determined based on the power demand of Fuel Cell Power System (FCPS) to the fuel cell stack (FCS). The average power demand was assumed to be 4.2 kW, based on the acquisition of the corresponding power request signal.

The hydrogen chemical power required can be calculated as:

$$P_{\text{H}_2} = \frac{P_{\text{FC}}}{\eta_{\text{FC}}}$$

where:

- P_{H_2} is the hydrogen chemical power (W),
- P_{FC} is the requested power from the fuel cell (W),

- η_{FC} is the fuel cell efficiency, assumed to be 50%.

Substituting the given values:

$$P_{\text{H}_2} = \frac{4.2 \times 10^3}{0.5} = 5 \times 10^3 \text{ W} = 8.4 \text{ kW} \tag{5.2}$$

The mass flow rate of hydrogen can be determined using the lower heating value (LHV) of hydrogen, which is 33.3 kWh/kg:

$$\dot{m}_{H_2} = \frac{P_{H_2}}{LHV_{H_2}} \tag{5.3}$$

$$\dot{m}_{\text{H}_2} = \frac{8.4}{33.3} = 0.150 \text{ kg/h} = 0.00007 \text{ kg/s} = 0.07 \text{ g/s} \tag{5.4}$$

Thus, the estimated hydrogen consumption rate is 0.15 g/s under the given operating conditions.

Mass and Moles Calculation

The flow rate is integrated over time to ascertain the total quantity of hydrogen utilized. The starting mass is diminished by this value to derive the current hydrogen mass $m_{\text{H}_2}(t)$. A logical condition is employed to guarantee that the mass remains non-negative and does not descend below a minimum threshold (e.g., 10^{-6}) to prevent numerical instability.

The current hydrogen mass is divided by the molar mass of hydrogen $M = 2.016\,\text{g/mol} = 2.016 \times 10^{-3}\,\text{kg/mol}$ to compute the number of moles:

$$n(t) = \frac{m_{\text{H}_2}(t)}{M} \tag{5.5}$$

The final outputs are:

- $m_{\text{H}_2}(t)$ – Current hydrogen mass in the tank [kg]
- $n(t)$ – Number of hydrogen moles [mol]

5.3 Tank Gas Temperature (Simulated): Thermal Model

The second block is the Tank Gas Temperature (Simulated) shown in Figure 5.4.

The Simulink model employed to compute the temperature within a hydrogen tank performs integral computations, incorporating multiple inputs and constants, each significantly affecting the thermal dynamics of the system. Here is a comprehensive analysis of these components.

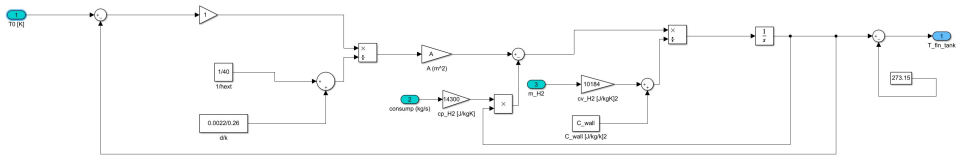

Figure 5.4. Tank Temperature H2. First simulation.

Thermal Contributions in the Hydrogen Tank Model

The evolution of the gas temperature inside the hydrogen tank is determined by the combined effect of different thermal contributions. The implemented model accounts for the following:

- **Convective heat exchange with the environment**
  This term models the heat flow from the tank to the surrounding air. It depends on the temperature difference between the ambient (T_{amb}) and the gas in the tank (T), as well as the overall thermal resistance of the tank wall. The corresponding term is:
  $$\dot{Q}_{\text{conv}} = h_{\text{eff}} \cdot A_{\text{wall}} \cdot (T_{\text{amb}} - T)$$
  where h_{eff} is the effective heat transfer coefficient (derived from convection and conduction through the wall layers), and A_{wall} is the surface area of the tank.

- **Cooling due to hydrogen outflow**
  As hydrogen exits the tank, it carries away thermal energy. This effect is modeled as:
  $$\dot{Q}_{\text{mass}} = \dot{m}_{\text{H}_2} \cdot c_p \cdot T$$
  where $\dot{m}_{\text{H}_2}$ is the mass flow rate of hydrogen, c_p is the specific heat at constant pressure, and T is the instantaneous gas temperature.

- **Thermal inertia of the system**
  The resistance of the tank to temperature variations is determined by its total heat capacity:
  $$C_{\text{total}} = m_{\text{H}_2} \cdot c_v + m_{\text{wall}} \cdot c_{p,\text{wall}}$$
  where c_v is the specific heat at constant volume of hydrogen, and $c_{p,\text{wall}}$ is the specific heat of the tank material.

- **Temperature variation**
  The net thermal effect is converted into a temperature derivative using the energy

balance:

$$\frac{dT}{dt} = \frac{1}{C_{\text{total}}} \left(h_{\text{eff}} \cdot A_{\text{wall}} \cdot (T_{\text{amb}} - T) - \dot{m}_{\text{H}_2} \cdot c_p \cdot T \right)$$

This equation is solved dynamically in Simulink using integrator blocks to obtain the gas temperature evolution $T(t)$.

5.3.1 Selection of Thermal Conductivity and Heat Transfer Coefficients

The precision of the thermal model relies on the correct selection of the thermal conductivity (k) of the tank materials and the heat transfer coefficients (h) for internal and exterior convection. These characteristics are essential for ascertaining the effective heat transfer coefficient $h_{\text{eff}} and, therefore, the temperature progression of the hydrogen storage system.$

5.3.2 Thermal Conductivity of the Tank Wall

Since the internal convective resistance is neglected, the dominant resistance to heat transfer comes from the conduction through the tank wall. The equivalent thermal conductivity of the tank wall, considering the liner and CFRP shell in series, is given by:

Material	**Thermal Conductivity k (W/mK)**
PA12 (Polyamide 12, liner)	0.2 - 0.3
PEEK (Polyether ether ketone, liner)	0.25 - 0.5
CFRP (Carbon Fiber Reinforced Polymer)	0.5 - 1.5
Epoxy Resin (matrix in CFRP)	0.2 - 0.3
Aluminum (liner, rare case)	120 - 160
Stainless Steel (if used in liner)	15 - 25

Table 5.1. Typical thermal conductivity values for tank materials [20].

$$k_{\text{wall}} = \frac{d_{\text{liner}} + d_{\text{CFRP}}}{\frac{d_{\text{liner}}}{k_{\text{liner}}} + \frac{d_{\text{CFRP}}}{k_{\text{CFRP}}}} \tag{5.6}$$

Using the material properties from Table 5.1, and given that:

- Liner thickness: $d_{\text{liner}} = 0.7$ mm,
- CFRP shell thickness: $d_{\text{CFRP}} = 0.15$ mm,
- Thermal conductivity of liner: $k_{\text{liner}} = 0.25$ W/mK,
- Thermal conductivity of CFRP: $k_{\text{CFRP}} = 0.3$ W/mK,

we obtain:

$$k_{\text{wall}} \approx 0.26 \text{ W/mK} \tag{5.7}$$

5.3.3 External Convective Heat Transfer Coefficient h_{ext}

The convective heat transfer coefficient between the tank's external wall and the ambient air is essential in the simplified model, as it signifies the principal mode of heat dissipation. Its value is contingent upon external conditions.

External Condition	h_{ext} **(W/m²K)**
Still air (natural convection)	2 - 10
Moving air (5 m/s, light wind)	10 - 30
High-speed airflow (20 m/s, fast driving)	30 - 100

Table 5.2. Typical values of h_{ext} for different external conditions.[7]

A plausible estimation for a hydrogen tank subjected to ambient air during vehicle operation is:

$$h_{\text{ext}} \approx 10 - 50 \text{ W/m}^2\text{K} \tag{5.8}$$

5.3.4 Final Parameter Selection for the Simplified Model

Based on the simplifications introduced, the following values are used in the simplified thermal model:

- Equivalent thermal conductivity of the tank wall: $k_{\text{wall}} = 0.28$ W/mK.
- External heat transfer coefficient: $h_{\text{ext}} = 10 - 50$ W/m²K.

These values ensure a balance between model accuracy and computational efficiency, allowing for a reduced complexity while still capturing the essential heat transfer dynamics.

5.3.5 Calculation of Specific Heat and Wall Mass

These values preserve equilibrium between model precision and computing efficiency, enabling less complexity while accurately representing the essential heat transport dynamics. Thermal equilibrium requires the determination of the specific heat capacity of the system's components:

- c_v, specific heat of hydrogen at constant volume;

- c_p, specific heat of solid materials (liner + CFRP);
- m_{wall}, total mass of the tank wall.

Specific Heat Capacity of Hydrogen c_v

Due to the confinement of hydrogen within the tank, which prevents volume expansion, the specific heat at constant volume is applicable.

$$c_v = 10.184\,\text{kJ/kgK} \tag{5.9}$$

5.3.6 Thermal Capacity of the Tank Wall

The overall thermal capacity of the tank wall, C_{wall}, is calculated by aggregating the contributions from the liner and the CFRP shell.

$$C_{\text{wall}} = m_{\text{liner}} c_{p,\text{liner}} + m_{\text{CFRP}} c_{p,\text{CFRP}} \tag{5.10}$$

where:

- $m_{\text{liner}} = 10.87$ kg is the mass of the liner,
- $c_{p,\text{liner}} = 1.8$ kJ/kgK represents the specific heat capacity of the liner at 298.15 K,
- $m_{\text{CFRP}} = 44.6$ kg represents the mass of the CFRP shell,
- $c_{p,\text{CFRP}} = 1.2$ kJ/kgK refers to the specific heat capacity of CFRP at 298.15 K.

Substituting the values:

$$C_{\text{wall}} = (10.87 \times 1.8) + (57.59 \times 1) = 77.156\ \text{kJ/K} \tag{5.11}$$

This result indicates that the total thermal capacity of the tank wall is around 77 kJ/K, meaning that an energy input of 75 kJ is required to increase its temperature by 1 K. This value is used in the thermal balance equation to determine the equilibrium temperature and the dynamic thermal properties of the hydrogen tank.

5.4 Tank Gas Pressure (Simulated)

Calculation of Pressure Using the Van der Waals Equation Finally, using the number of moles $n_{\text{H}_2}(t)$, the pressure inside the tank can be calculated with the Van der Waals equation (Figure 5.5):

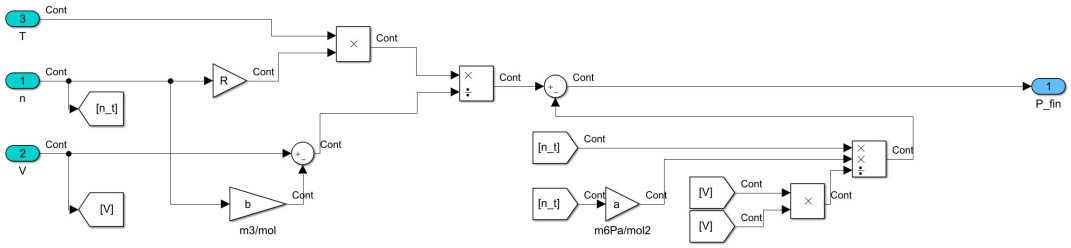

Figure 5.5. Tank Gas Pressure Calculation

$$\left(P + a\frac{n^2}{V^2}\right)(V - nb) = nRT \tag{5.12}$$

Solving the The Van der Waals equation to compute the tank pressure P,i get:

$$P = \frac{nRT}{V - nb} - a\left(\frac{n}{V}\right)^2 \tag{5.13}$$

where:

- P is the tank pressure (Pa),
- V is the tank volume (m^3),
- n is the number of hydrogen moles calculated previously,
- $R = 8.314 J\,mol^{-1}\,K^{-1}$ is the universal gas constant,
- T is the absolute temperature of hydrogen (K),
- $a = 0.0244 m^6 Pa/mol^2$ and $b = 2.65 \times 10^{-5} m^3/mol$ are the Van der Waals constants for hydrogen.

This equation is calculated numerically at each time step to determine the actual hydrogen pressure within the tank, accounting for molecular interactions and gas compressibility.

5.5 Pressure Regulator

Operation of the Pressure Regulator: The pressure regulator reduces and stabilizes the pressure of a gas (in this case, hydrogen) from a high initial value (e.g., 700 bar) to a

manageable level for the downstream system (e.g., 12.5 bar). This regulation is crucial to ensure safety and proper functioning of the system, such as a fuel cell.

The goal is to predict the dynamic behavior of the pressure regulator. The modeling aims to size the orifice area and the downstream volume to ensure stable pressure. To model the pressure regulator more realistically, two key aspects are considered:

- How the regulator responds to variable flow demands,
- How it ensures stability and optimal performance across the entire operational range. The more realistic model includes: a variable orifice to dynamically manage flow, a dual-stage regulator to stabilize downstream pressure, and active pressure control to optimize the response to load variations.

5.5.1 Basic Physical Principles

In a pressure regulator, the hydrogen expansion process can be modeled as both adiabatic (no heat exchange) and isenthalpic (constant enthalpy). Under the assumptions of no heat transfer ($\dot{Q} = 0$) and no mechanical work ($\dot{W} = 0$), the total energy of the gas remains constant during expansion.

However, this is not an isentropic process, as entropy increases due to internal dissipations and turbulence generated within the valve. Unlike turbines, no useful mechanical work is produced, and irreversibilities dominate.

The total enthalpy of a gas is defined as the sum of its static enthalpy h and the kinetic energy associated with its velocity:

$$h_0 = h + \frac{v^2}{2}$$

If the gas accelerates through the orifice, part of the static enthalpy is converted into kinetic energy, resulting in a temperature drop. Conversely, if the gas decelerates downstream, the kinetic energy is partially recovered as internal energy, increasing the gas temperature.

The static enthalpy h represents the energy content per unit mass of fluid, composed of:

- The internal energy u, associated with the microscopic motion of gas molecules,
- The flow energy Pv, related to the fluid's capacity to perform work during expansion or compression.

From the definition:

$$h = u + Pv$$

For an ideal gas, using the equation of state $Pv = RT$, we get:

$$h = u + RT$$

Taking the differential with respect to temperature:

$$dh = du + R\,dT$$

Since $du = C_v\,dT$, we obtain:

$$dh = C_v\,dT + R\,dT = (C_v + R)\,dT$$

Defining the specific heat at constant pressure as $C_p = C_v + R$, we finally get:

$$h = C_p T$$

Total enthalpy is commonly used to analyze high-speed fluid systems (e.g., turbines, compressors, gas jets). In contrast, static enthalpy is suitable for low-speed flows where kinetic energy is negligible compared to internal energy. In this study, we use static enthalpy due to the relatively low hydrogen velocity across the regulator.

Isenthalpic Expansion in the Regulator In the case of an isenthalpic process:

$$h_{\text{up}} = h_{\text{down}}$$

Expressing enthalpy as a function of temperature and pressure:

$$dh = \left(\frac{\partial h}{\partial T}\right)_P dT + \left(\frac{\partial h}{\partial P}\right)_T dP = 0$$

Since enthalpy remains constant ($dh = 0$), we obtain:

$$\left(\frac{\partial h}{\partial T}\right)_P dT = -\left(\frac{\partial h}{\partial P}\right)_T dP$$

Recognizing that $\left(\frac{\partial h}{\partial T}\right)_P = C_p$, the Joule-Thomson coefficient is defined as:

$$\mu_{JT} = \frac{1}{C_p}\left(\frac{\partial h}{\partial P}\right)_T$$

Substituting:

$$C_p dT = -\left(\frac{\partial h}{\partial P}\right)_T dP$$

Integrating from upstream to downstream:

$$\int_{T_{\text{up}}}^{T_{\text{down}}} dT = \int_{P_{\text{up}}}^{P_{\text{down}}} \mu_{JT} dP$$

Assuming that μ_{JT} is constant over the pressure interval, the temperature after expansion is given by:

$$T_{\text{down}} = T_{\text{up}} + \mu_{JT}(P_{\text{down}} - P_{\text{up}})$$

5.6 Multi-Stage Pressure Regulator Model in MATLAB/Simulink

The multi-stage pressure regulator is designed to gradually reduce hydrogen pressure from 700 bar (storage tank pressure) to the typical fuel cell operating range, usually between 10 bar and 25 bar. A technical datasheet for a two-stage pressure regulator is available on the manufacturer's website [16].

This stepwise pressure reduction is essential to prevent excessive cooling caused by the Joule-Thomson effect and to ensure stable and controlled hydrogen flow to the fuel cell system.

In this analysis, based on the technical specifications of the selected pressure regulator, the final downstream pressure is set to 12.5 bar. This pressure is maintained constant throughout the operation.

5.6.1 Structure and Implementation of the Pressure Regulator Model

The pressure regulator model simulates a three-stage hydrogen pressure reduction process. Its objective is to reduce the inlet hydrogen pressure, typically around 700 bar, to a target output pressure of 12.5 bar, as required by the fuel cell stack. The model includes key thermodynamic effects such as gas cooling due to the Joule–Thomson expansion and manages both subcritical and choked flow conditions. The regulator ensures a stable mass flow rate while computing the required orifice areas at each stage.

Physical Parameters. The model uses typical hydrogen gas properties:

- $\gamma = 1.41$ – ratio of specific heats,
- $R = 4124\,\text{J/(kg} \cdot \text{K)}$ – specific gas constant,
- $C_d = 0.7$ – discharge coefficient of the orifices,

- μ_{JT} – Joule–Thomson coefficients for each stage, based on empirical data [17].

Initial Setup. The function receives the upstream pressure P_{up}, temperature T_{up}, and desired mass flow rate $\dot{m}_{\mathrm{target}}$ as inputs. It returns the intermediate and final pressures and temperatures, the effective orifice areas for each stage, and the calculated flow rate.

5.6.2 Orifice Area Calculation in Subcritical and Choked Flow Conditions

In the design of pressure regulators, the orifice area must be calculated to ensure that the desired mass flow rate is delivered under the given pressure and temperature conditions. The equations vary depending on whether the flow is subcritical (non-choked) or choked (sonic). The transition between the two regimes occurs when the downstream-to-upstream pressure ratio falls below the critical threshold:

$$\frac{P_{\mathrm{down}}}{P_{\mathrm{up}}} \leq \left(\frac{2}{\gamma+1}\right)^{\frac{\gamma}{\gamma-1}}$$

5.6.3 Step-by-Step Derivation of the Orifice Area Equations

The objective is to determine the orifice area A required to achieve a given mass flow rate $\dot{m}$ of a compressible gas, such as hydrogen, under specific upstream conditions. Two distinct regimes must be considered: subcritical (non-choked) flow and choked (critical) flow. The derivations are based on the principles of conservation of mass, momentum, and energy, under steady and adiabatic flow assumptions.

First Stage – Subcritical Flow. In the first stage, the intermediate pressure P_{mid} is iteratively increased until the pressure ratio $\frac{P_{\mathrm{mid}}}{P_{\mathrm{up}}}$ exceeds the critical value for hydrogen, approximately 0.528. This guarantees subsonic conditions and avoids choked flow. In this regime, the gas does not reach the speed of sound while passing through the orifice. The downstream pressure still influences the mass flow rate. Once that the final and initial stage pressures are set, the orifice area is calculated using:

$$A = \frac{\dot{m}}{C_d \cdot \sqrt{2\rho(P_{\mathrm{up}} - P_{\mathrm{mid}})}} \tag{5.14}$$

This equation comes from the following calculations.
By starting from the energy balance for a steady, adiabatic flow:

$$\frac{v^2}{2} = \frac{P_{\mathrm{up}} - P_{\mathrm{down}}}{\rho} \tag{5.15}$$

Solving for the velocity:

$$v = \sqrt{\frac{2(P_{\text{up}} - P_{\text{down}})}{\rho}} \tag{5.16}$$

The mass flow rate is defined as:

$$\dot{m} = \rho \cdot A \cdot v \tag{5.17}$$

Substituting the expression for v:

$$\dot{m} = \rho \cdot A \cdot \sqrt{\frac{2(P_{\text{up}} - P_{\text{down}})}{\rho}} = A \cdot \sqrt{2\rho(P_{\text{up}} - P_{\text{down}})} \tag{5.18}$$

Including the discharge coefficient C_d to account for non-ideal effects:

$$\dot{m} = C_d \cdot A \cdot \sqrt{2\rho(P_{\text{up}} - P_{\text{down}})} \tag{5.19}$$

Solving for the area:

$$A = \frac{\dot{m}}{C_d \cdot \sqrt{2\rho(P_{\text{up}} - P_{\text{down}})}} \tag{5.20}$$

The density ρ is obtained from the ideal gas law:

$$\rho = \frac{P_{\text{up}}}{RT_{\text{up}}} \tag{5.21}$$

5.6.4 Step-by-Step Derivation of the Orifice Area in Choked Flow Conditions

In this section, it is derived the expression for the minimum cross-sectional area A required to achieve a desired mass flow rate $\dot{m}$ in the case of choked flow. Choked flow occurs when the velocity of the gas at the throat of the orifice reaches the speed of sound ($M = 1$), and further reductions in downstream pressure do not increase the flow rate.

1. Starting from the Continuity Equation

The mass flow rate for a compressible fluid is given by:

$$\dot{m} = \rho \cdot A \cdot v \tag{5.22}$$

where:

- $\dot{m}$ is the mass flow rate [kg/s],
- ρ is the gas density at the throat [kg/m^3],
- A is the orifice area [m^2],
- v is the flow velocity at the throat [m/s].

Second Stage – Choked Flow. The second stage reduces the pressure by a fixed ratio of 10:1, setting $P_2 = P_{\text{mid}}/10$. Since the resulting pressure ratio is lower than 0.528, the flow is considered choked (sonic). The orifice area is computed using the isentropic flow relation:

$$A = \frac{\dot{m}}{C_d P_{\text{mid}}} \cdot \sqrt{\frac{\gamma}{RT_{\text{mid}}} \left(\frac{2}{\gamma+1}\right)^{\frac{\gamma+1}{\gamma-1}}} \tag{5.23}$$

In choked conditions, the velocity v at the orifice equals the local speed of sound a:

$$v = a = \sqrt{\gamma RT} \tag{5.24}$$

Substitute into the mass flow rate equation:

$$\dot{m} = \rho \cdot A \cdot \sqrt{\gamma RT} \tag{5.25}$$

3. Expressing Density in Terms of Stagnation Conditions

Using isentropic relations for an ideal gas, the density at the throat under choked conditions ($M = 1$) can be expressed as a function of the stagnation (upstream) pressure and temperature:

$$\rho = \frac{P}{RT} \quad \Rightarrow \quad \rho^* = \frac{P^*}{RT^*} \tag{5.26}$$

P^* and T^* (static conditions at the throat) are expressed in terms of the stagnation (total) conditions P_0 and T_0 using isentropic relations:

$$\frac{T^*}{T_0} = \frac{2}{\gamma+1} \tag{5.27}$$

$$\frac{P^*}{P_0} = \left(\frac{2}{\gamma+1}\right)^{\frac{\gamma}{\gamma-1}} \tag{5.28}$$

Substituting into the expression for density:

$$\rho^* = \frac{P_0}{RT_0} \cdot \left(\frac{2}{\gamma+1}\right)^{\frac{\gamma}{\gamma-1}} \cdot \left(\frac{\gamma+1}{2}\right) = \frac{P_0}{RT_0} \cdot \left(\frac{2}{\gamma+1}\right)^{\frac{1}{\gamma-1}} \tag{5.29}$$

4. Substituting Everything Back

Inserting this into the mass flow rate equation:

$$\dot{m} = \rho^* \cdot A \cdot \sqrt{\gamma R T^*} \tag{5.30}$$

Replacing T^* with $T_0 \cdot \frac{2}{\gamma+1}$ and use the expression for ρ^* found above:

$$\dot{m} = \left[\frac{P_0}{RT_0} \cdot \left(\frac{2}{\gamma+1} \right)^{\frac{1}{\gamma-1}} \right] \cdot A \cdot \sqrt{\gamma R T_0 \cdot \frac{2}{\gamma+1}} \tag{5.31}$$

Simplifying: Separate terms inside the square root:

$$\sqrt{\gamma R T_0 \cdot \frac{2}{\gamma+1}} = \sqrt{\gamma R T_0} \cdot \sqrt{\frac{2}{\gamma+1}} \tag{5.32}$$

Final form:

$$\dot{m} = A \cdot P_0 \cdot \sqrt{\frac{\gamma}{RT_0}} \cdot \left(\frac{2}{\gamma+1} \right)^{\frac{\gamma+1}{2(\gamma-1)}} \tag{5.33}$$

5. Solving for the Area

Rearranging to solve for A:

$$A = \frac{\dot{m}}{P_0} \cdot \sqrt{\frac{RT_0}{\gamma}} \cdot \left(\frac{2}{\gamma+1} \right)^{-\frac{\gamma+1}{2(\gamma-1)}} \tag{5.34}$$

Including the discharge coefficient C_d to account for real effects:

$$A = \frac{\dot{m}}{C_d \cdot P_0} \cdot \sqrt{\frac{RT_0}{\gamma}} \cdot \left(\frac{2}{\gamma+1} \right)^{-\frac{\gamma+1}{2(\gamma-1)}} \tag{5.35}$$

Which is the standard engineering expression for the **critical orifice area**.

Interpretation. This result shows that, under choked conditions:

- The required area is directly proportional to the mass flow rate,
- It is inversely proportional to the upstream pressure,
- It depends on the gas temperature and properties (γ, R),
- The downstream pressure does not appear in the equation — confirming that in choked flow, the mass flow is unaffected by it.

Engineering Implication. In designing hydrogen regulators, when a stage operates under choked flow, this equation allows precise sizing of the orifice to deliver the target mass flow rate. Since the flow is independent of downstream fluctuations, it provides a stable and predictable behavior — which is particularly valuable in automotive applications, where demand may vary rapidly.

5.6.5 Detailed Description of the `pressure_regulator` Function

The `pressure_regulator` function implements a numerical model of a three-stage pressure regulator for hydrogen gas, intended for fuel cell vehicle applications. The goal is to reduce the inlet pressure P_{up} to a specified final pressure of 12.5 bar, while delivering a target mass flow rate $\dot{m}_{\text{target}}$, considering the thermodynamic behavior of the gas and the presence of choked flow.

Function Inputs and Outputs. The function takes as input:

- P_{up} – inlet pressure [Pa],
- T_{up} – inlet temperature [K],
- $\dot{m}_{\text{target}}$ – desired mass flow rate [kg/s].

It returns the intermediate and final pressures and temperatures, the calculated orifice areas for each stage, and the computed mass flow rate.

Physical Constants. The model uses:

- $\gamma = 1.41$ – specific heat ratio for hydrogen,
- $R = 4124\,\text{J/(kg} \cdot \text{K)}$ – specific gas constant for hydrogen,
- $C_d = 0.7$ – discharge coefficient,
- $\mu_{\text{JT},1}, \mu_{\text{JT},2}$ – Joule-Thomson coefficients for cooling effects in the respective stages.

Initial Conditions. The final pressure P_{down} is set to 12.5 bar (converted to Pascals), and a first estimate of the intermediate pressure P_{mid} is computed as the geometric mean between inlet and outlet pressures. Initial orifice areas are set to very small values (10^{-8} m^2) and refined later.

First Stage – Subcritical Flow. To avoid choked flow in the first stage, the function iteratively increases P_{mid} until the pressure ratio $P_{\text{mid}}/P_{\text{up}}$ exceeds the critical threshold of 0.528. This ensures that the first expansion is subsonic. The gas density is then calculated using the ideal gas law:

$$\rho_{\text{up}} = \frac{P_{\text{up}}}{RT_{\text{up}}} \tag{5.36}$$

The orifice area for the first stage is computed using the subcritical flow formula:

$$A_1 = \frac{\dot{m}_{\text{target}}}{C_d\sqrt{2\rho_{\text{up}}(P_{\text{up}} - P_{\text{mid}})}} \tag{5.37}$$

The actual mass flow rate is calculated accordingly. The temperature at the outlet of the first stage is adjusted with the Joule-Thomson effect:

$$T_{\text{mid}} = T_{\text{up}} + \mu_{\text{JT},1}(P_{\text{mid}} - P_{\text{up}}) \tag{5.38}$$

Second Stage – Choked Flow. The second stage reduces the pressure by a fixed 10:1 ratio:

$$P_2 = \frac{P_{\text{mid}}}{10} \tag{5.39}$$

The temperature is updated using:

$$T_2 = T_{\text{mid}} + \mu_{\text{JT},2}(P_2 - P_{\text{mid}}) \tag{5.40}$$

If the ratio P_2/P_{mid} is below 0.528, choked flow is assumed, and the orifice area is calculated using the isentropic sonic flow equation:

$$A_2 = \frac{\dot{m}_{\text{target}}}{C_d \cdot P_{\text{mid}}} \cdot \sqrt{\frac{RT_{\text{mid}}}{\gamma} \cdot \left(\frac{2}{\gamma+1}\right)^{\frac{-(\gamma+1)}{\gamma-1}}} \tag{5.41}$$

Otherwise, the subcritical formula is used again:

$$A_2 = \frac{\dot{m}_{\text{target}}}{C_d \cdot \sqrt{2\rho_{\text{mid}}(P_{\text{mid}} - P_2)}} \tag{5.42}$$

Third Stage – Final Pressure Reduction. The third stage reduces the pressure from P_2 to the final value:

$$P_{\text{down}} = \frac{P_2}{3} \tag{5.43}$$

The temperature is adjusted via:

$$T_{\text{down}} = T_2 + \mu_{\text{JT},2}(P_{\text{down}} - P_2) \tag{5.44}$$

As before, if $P_{\text{down}}/P_2 < 0.528$, choked flow is assumed, and the orifice area is calculated with:

$$A_3 = \frac{\dot{m}_{\text{target}}}{C_d \cdot P_2} \cdot \sqrt{\frac{RT_2}{\gamma} \cdot \left(\frac{2}{\gamma+1}\right)^{\frac{-(\gamma+1)}{\gamma-1}}} \tag{5.45}$$

Otherwise, the subcritical formula applies:

$$A_3 = \frac{\dot{m}_{\text{target}}}{C_d \cdot \sqrt{2\rho_2(P_2 - P_{\text{down}})}} \tag{5.46}$$

Summary. This function provides a simplified but realistic model for sizing and simulating a multi-stage pressure regulator for hydrogen. Each stage is treated individually, and both thermodynamic effects (via Joule-Thomson cooling) and aerodynamic limitations (via choked flow) are taken into account. The model helps identify the required orifice geometries to deliver the specified mass flow rate under given operating conditions.

Conclusion. This model enables a practical and physically accurate simulation of a multi-stage pressure regulator operating under real hydrogen conditions. It allows proper sizing of orifices for each stage, ensuring compliance with the expected flow rate while accounting for thermal effects and flow regimes. The use of Joule–Thomson corrections and critical flow evaluation makes the model particularly suitable for hydrogen fuel cell vehicle applications.

5.6.6 Results and System Behavior

The simulation results confirm that:

- The first stage operates in a controlled subcritical regime.
- The second stage reaches critical flow, where mass flow is dictated by upstream conditions.
- The final temperature of the hydrogen is computed using the Joule-Thomson effect.

This model provides a representation of the fuel cell vehicle's pressure regulation system, balancing control stability and computational efficiency.

Chapter 6

Second and Third Simulations

6.1 Second Simulation: Introduction of the State Valve

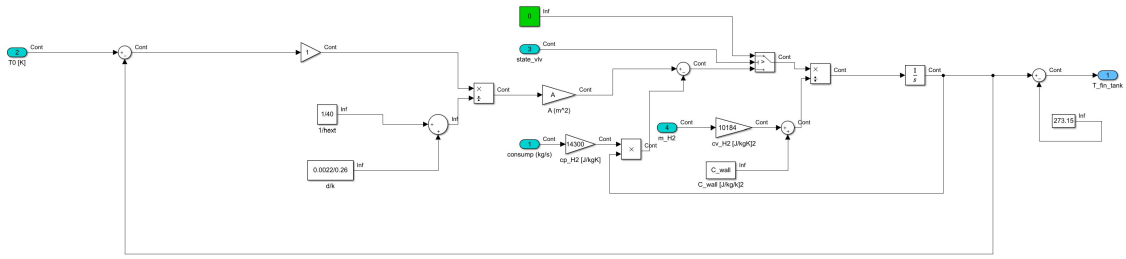

Figure 6.1. Tank Gas Temperature (Simulated)

Adjusted Description for Simulation Approach

In the updated model for the Simulink system (Figure 6.1), the valve operation is directly controlled by the *mode actual* signal from the Fuel Cell Power System (FCPS). The system's configuration ensures that the valve's behavior is responsive to operational states and monitored environmental conditions:

Second Simulation: Valve State Influence on Convective Heat Transfer

In the second simulation scenario, the state of the hydrogen valve is introduced as an additional control input. This signal, denoted as `state_vlv`, determines whether the valve is in a closed state (value = 1, no flow requested) or an open state (value = 0, flow requested).

When the valve is in state 1 (no flow), the hydrogen remains confined within the tank, and there is no mass exchange with the external system. The term $Q_{\text{out}} = \dot{m}_{\text{H2}} \cdot c_{p,\text{H2}} \cdot T$ represents the heat loss due to the mass flow of hydrogen exiting the tank. In the model, this contribution is considered only when the valve connecting the hydrogen tank to the downstream system is open.

To reflect this behavior, the mass flow rate $\dot{m}_{\text{H2}}$ is multiplied by a binary signal `state_vlv`, which takes the value 1 when the valve is open and 0 when it is closed. As a result, Q_{out} is zero during phases where the valve is closed, meaning there is no mass leaving the tank. This allows the simulation to accurately represent the thermal behavior of the system in both operating and idle phases.

6.2 Final Simulation: Variable Power and Speed Dependency

6.2.1 Third Simulation: Power-Dependent Hydrogen Flow

In the third simulation, the power requested by the fuel cell is no longer considered constant but varies over time. This value is used to calculate the hydrogen mass flow rate, which becomes a function of time as well. The relation used to compute the flow rate is the following:

$$\dot{m}_{\text{H}_2}(t) = \frac{P_{\text{FC}}(t)}{\eta \cdot \text{LHV}_{\text{H}_2}} \tag{6.1}$$

In this expression:

- $\dot{m}_{\text{H}_2}(t)$ is the hydrogen mass flow rate at a given time,
- $P_{\text{FC}}(t)$ is the fuel cell power demand,
- η is the overall efficiency of the system,
- LHV_{H_2} is the lower heating value of hydrogen.

The time-dependent flow rate is used to determine the mass of hydrogen in the tank, which becomes one of the inputs to the block responsible for calculating the gas temperature. In this way, the thermal behavior of the tank is directly influenced by the power demand, resulting in a more dynamic and realistic simulation.

The power required by Fuel Cell Control Unit (FCCU) varies over time according to the driving profile. This signal is passed to the Fuel Cell Power System (FCPS) and used to calculate the hydrogen mass flow rate, which becomes a function of time. The

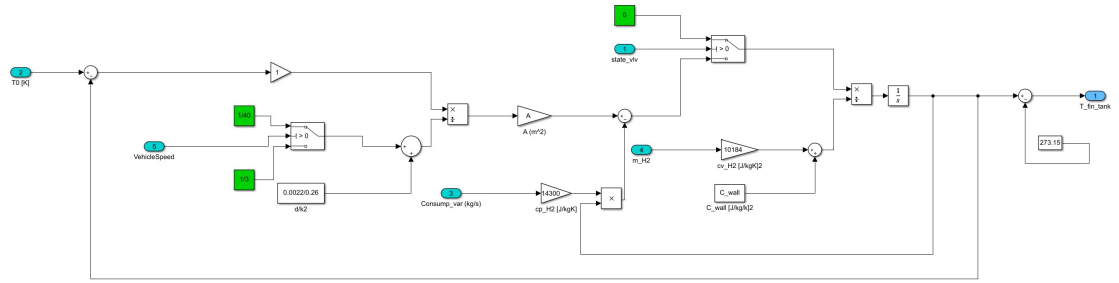

Figure 6.2. Tank Gas Temperature (Simulated)

computed flow rate is then used to update the hydrogen mass inside the tank, which serves as an input to the *Tank Gas Temperature (Simulated)* block (Figure 6.2). This allows the gas temperature to respond dynamically to the actual operating conditions of the fuel cell.

Moreover, the simulation also considers the influence of vehicle speed. When the vehicle is in motion, the external convective heat transfer coefficient assumes a typical value consistent with forced convection. Conversely, when the vehicle is stationary, the coefficient is reduced to reflect the limited air movement around the tank (around 1/3 $\frac{W}{m^2K}$). This variation affects the thermal exchange with the environment, making the temperature evolution more representative of real operating conditions.

Chapter 7

Results

7.1 Summary of the Three Simulation Scenarios

The simulation model was used to evaluate three different scenarios, each introducing increasing levels of complexity and realism in the representation of the hydrogen storage system.

All simulations started under the assumption of thermal equilibrium among the external environment, the tank walls, and the gas contained within the tank. The initial temperature was established at 15°C (288.15K), aligning with the experimental results obtained from real-world testing.

7.1.1 First Simulation Results: Constant Hydrogen Consumption

The final graphs for temperature and pressure within the fuel cell system are depicted in the figures below. 7.1 and 7.2. These graphs represent the simulation outputs and are compared with actual data derived from real signal acquisitions taken from a vehicle. This comparison is essential for validating the simulation model against real-world conditions to ensure its accuracy and reliability in operational settings.

These figures illustrate the effectiveness of the simulation in replicating the actual behavior of the system under typical operational conditions. Discrepancies, if any, are analyzed to refine the model, enhancing its predictive accuracy and reliability.

A constant mass flow rate of hydrogen is assumed in the first scenario. The simulation examines the temperature and pressure dynamics of the tank over time, excluding valve control and vehicle dynamics. This scenario offers a simplified foundation for comprehending the essential gas behavior within the tank.

In the graph 7.1, the temperature demonstrates exponential decay, commencing immediately due to the simplification that disregards both valve dynamics and the delayed

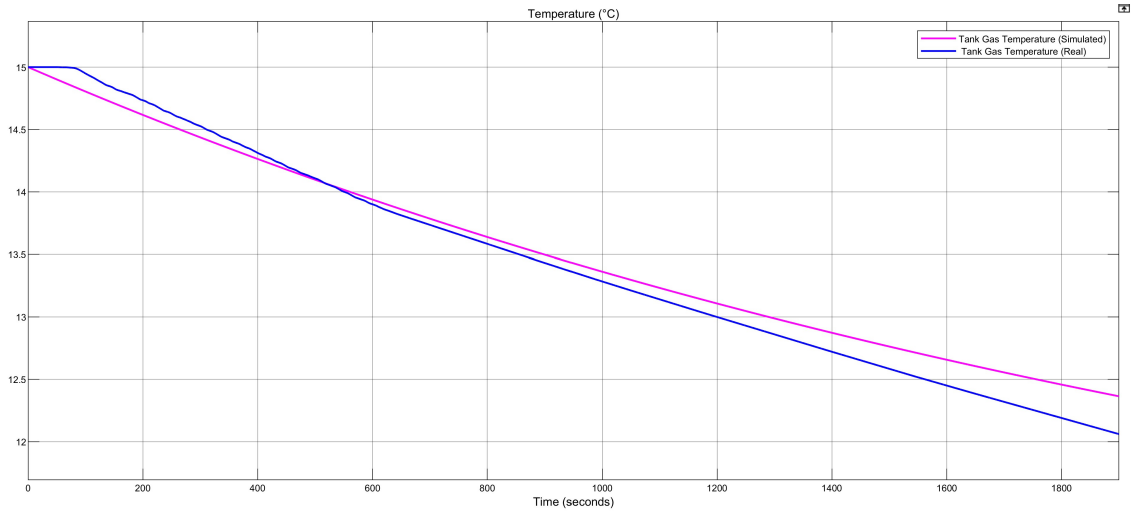

Figure 7.1. Comparison of simulated temperature data with real temperature data acquired from the vehicle.

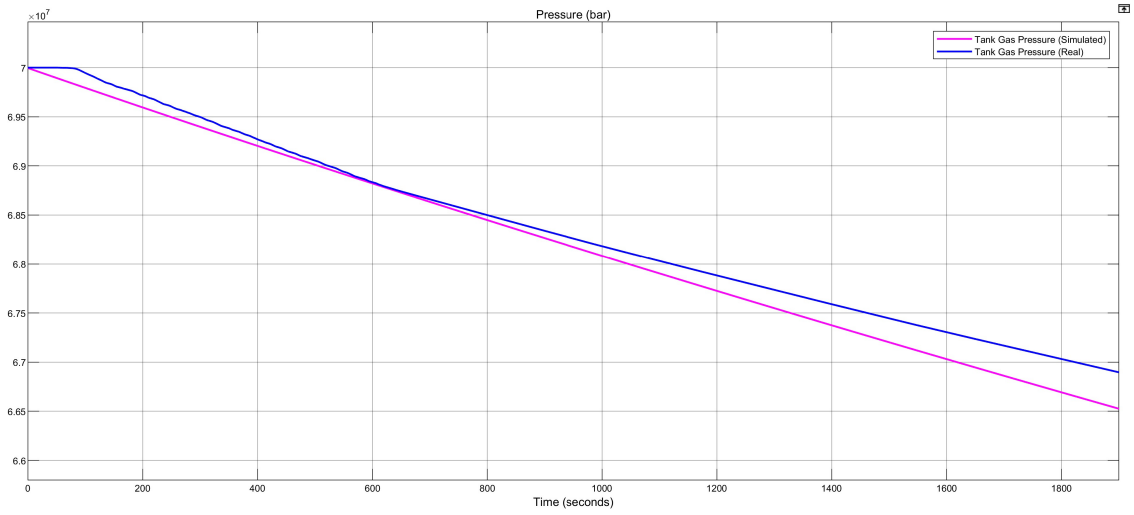

Figure 7.2. Comparison of simulated pressure data with real pressure data acquired from the vehicle.

release of hydrogen from the tank. The final temperature value diverges from the actual observed value by approximately 0.4°C.

The variation in pressure, in the graph 7.2, is predominantly influenced by the change in the amount of moles of hydrogen in the tank, rather than by temperature. During a 30-minute interval, the temperature diminishes by merely 3°C, yet the pressure declines

by roughly 3.35 bar. This indicates that the pressure decline is primarily attributable to the slow liberation of hydrogen, rather than thermal influences.

7.1.2 Second Simulation Results: Influence of Valve State

The second scenario introduces the effect of the hydrogen valve state. When the valve is closed, the hydrogen remains confined within the tank and there is no mass exchange with the external system. The Qout is not considered when the valve is closed. The simulation dynamically adjusts the contribution of the thermal loss based on the valve status, allowing for more accurate modeling of the tank temperature.

The pressure graph (graph 7.4) erroneously depicts a decline from the outset of the simulation, instead of appropriately reflecting the valve opening. This mismatch originates from the modeling assumption of a constant hydrogen mass flow rate implemented from the outset. The temperature only begins to decline once the physical outflow commences, whereas pressure is more promptly affected by the alteration in the quantity of moles. In this simulation, the quantity of moles is presumed to diminish continuously over time, calculated by integrating a constant mass consumption rate and dividing by the molar mass of hydrogen. Thus, the model indicates an immediate decrease in pressure, despite the postponement of hydrogen emission.

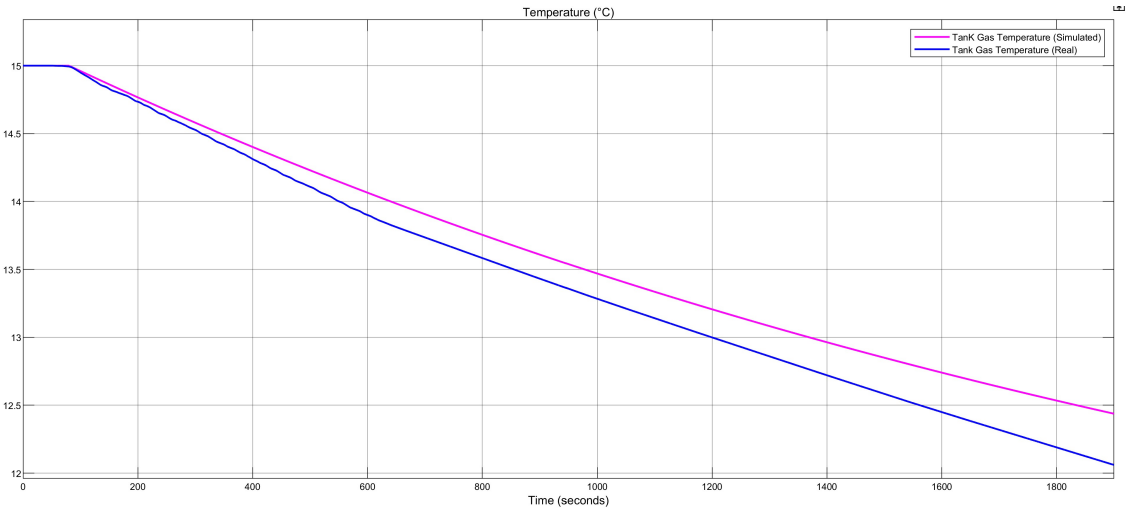

Figure 7.3. Comparison of simulated temperature data with real temperature data acquired from the vehicle.

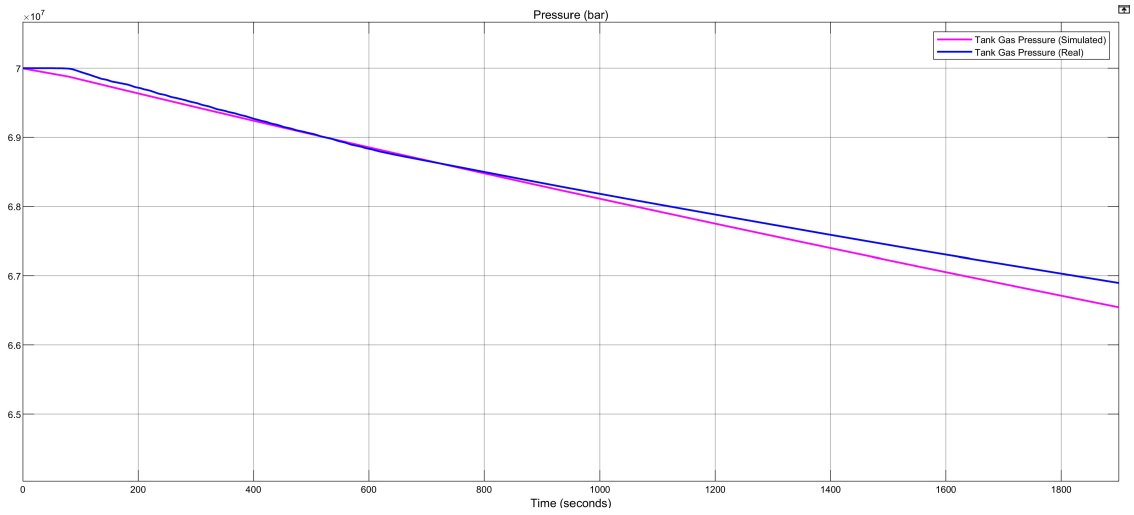

Figure 7.4. Comparison of simulated pressure data with real pressure data acquired from the vehicle.

7.1.3 Final Simulation Results - Variable Power and Vehicle Speed

In the final scenario, the power demanded by the Fuel Cell System varies over time and is used to determine a time-dependent hydrogen flow rate. This affects the hydrogen mass in the tank and, subsequently, the interior temperature. Furthermore, vehicle speed is taken into account: when the vehicle is stationary, external convection decreases, resulting in a reduced heat transfer rate. This configuration enables the model to more accurately simulate actual driving circumstances.

Third Simulation – Temperature Analysis

In this third simulation, the behavior of the tank gas temperature (Figure 7.5) shows a better agreement with the real data. The improvement is mainly due to two key enhancements introduced in the model:

1. **Reduction of h_{eff} after 600 seconds:**
   When the vehicle is immobile, forced convection stops and natural convection prevails. The effective heat transfer coefficient, h_{eff}, diminishes after 600 seconds, resulting in decreased heat exchange with the external environment. The heat gain term is:

$$Q_{\text{in}} = h_{\text{eff}} \cdot A \cdot (T_{\text{amb}} - T)$$

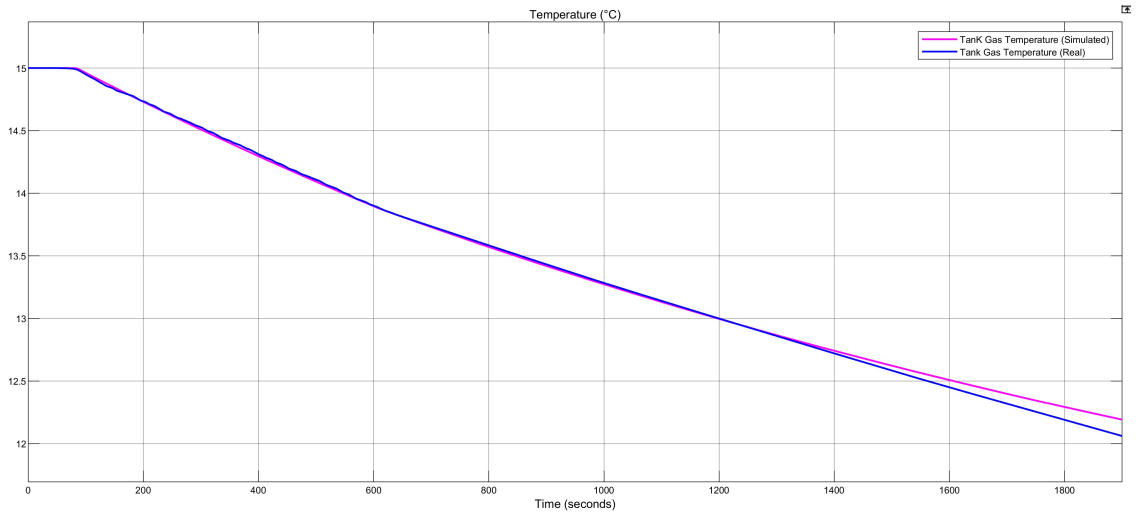

Figure 7.5. Comparison of simulated temperature data with real temperature data acquired from the vehicle.

A lower h_{eff} results in a reduced thermal energy input from the environment. Moreover, a lower h_{eff} also attenuates the exponential temperature decay.

2. **Time-varying hydrogen mass flow rate:**
   The hydrogen flow rate is not constant but computed from a time-dependent power profile. This means that:
   $$Q_{\text{out}} = \dot{m}_{\text{H2}} \cdot c_p \cdot T$$
   is also variable. During high-power phases, such as start-up and motion, hydrogen consumption increases, leading to enhanced cooling. After stopping of the vehicle, the power diminishes, resulting in a corresponding reduction in hydrogen flow, which slightly decreases the cooling contribution. Despite this, this cooling factor continues to prevail in the thermal equilibrium.

3. **Thermal balance dynamics:**
   The temperature evolution is governed by the following first-order differential equation:
   $$\frac{dT}{dt} = \frac{1}{C_{\text{tot}}} \left(h_{\text{eff}} \cdot A \cdot (T_{\text{amb}} - T) - \dot{m}_{\text{H2}} \cdot c_p \cdot T \right)$$
   This equation includes two opposing thermal contributions:

   - $h_{\text{eff}} \cdot A \cdot (T_{\text{amb}} - T)$: represents the **heating effect** from the ambient.
   - $\dot{m}_{\text{H2}} \cdot c_p \cdot T$: represents the **cooling effect** due to hydrogen outflow.

When the vehicle stops and h_{eff} is reduced, the heating effect is also diminished. Nevertheless, the cooling effect remains more significant, even if reduced due to the lower hydrogen flow. This explains why the tank temperature continues to decrease, though with a less pronounced slope.

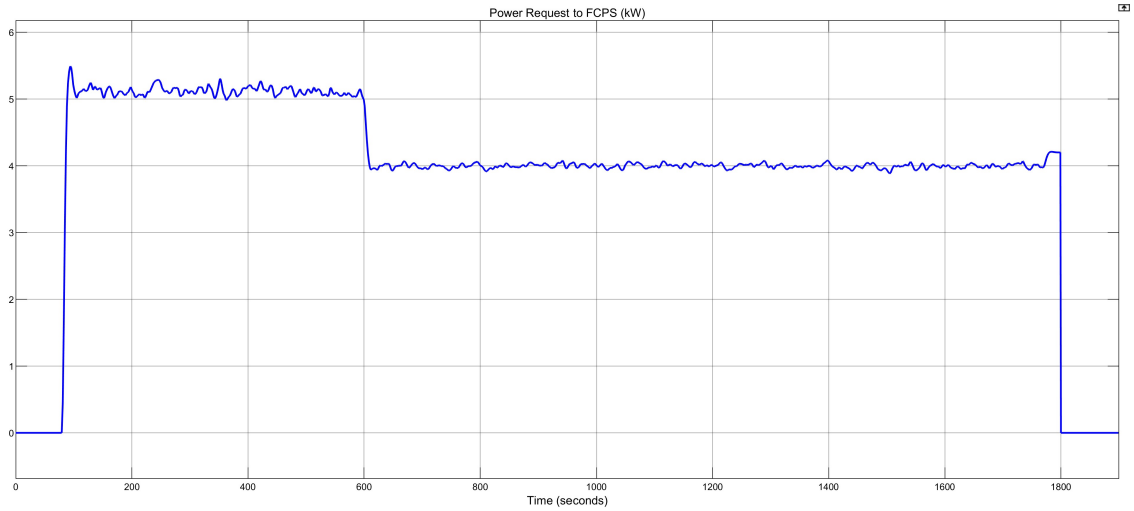

Figure 7.6. Power request to FCPS (acquired via CAN)

4. **Power contribution during shutdown:**
   Despite the FCPS (Fuel Cell Power System) power request signal declining to zero toward the simulation's conclusion—indicating the mode actual signal entering the shutdown state—a residual auxiliary load persists, resulting in ongoing hydrogen consumption: a small auxiliary power has been assumed. This auxiliary load, though reduced, still requires the fuel cell to remain active and draws hydrogen from the tank.
   In fact, the real FCPS power signal acquired via CAN (Figure 7.6) shows a small spike just before shutting down. This behavior is typical and used for final safety checks or purging procedures before fuel cell deactivation.

Conclusion:

This simulation accurately captures the complex interplay between thermal input and output. By introducing a variable hydrogen flow rate and adjusting the heat transfer coefficient based on vehicle dynamics, the simulated temperature closely replicates the actual behavior observed in the experimental data.

The curve's shape concerning pressure (Figure 7.7) is affected by the introduction of a

time-dependent power demand, from which the hydrogen flow rate is determined. Upon the vehicle's cessation, the power demand from the Fuel Cell System diminishes, resulting in a reduced hydrogen consumption rate. Consequently, the reduction in the number of moles within the tank decelerates, leading to a less pronounced decline in pressure. This clarifies the irregular pressure decline noted in relation to variations in the driving cycle.

The pressure is calculated using the Van der Waals equation:

$$\left(P + a\left(\frac{n}{V}\right)^2\right)(V - nb) = nRT$$

Solving for pressure:

$$P = \frac{nRT}{V - nb} - a\left(\frac{n}{V}\right)^2$$

This expression shows that pressure is non-linearly dependent on the number of moles n, especially at high densities. Therefore, any variation in the hydrogen outflow rate—determined by the time-dependent power demand—leads to a corresponding non-uniform change in pressure.

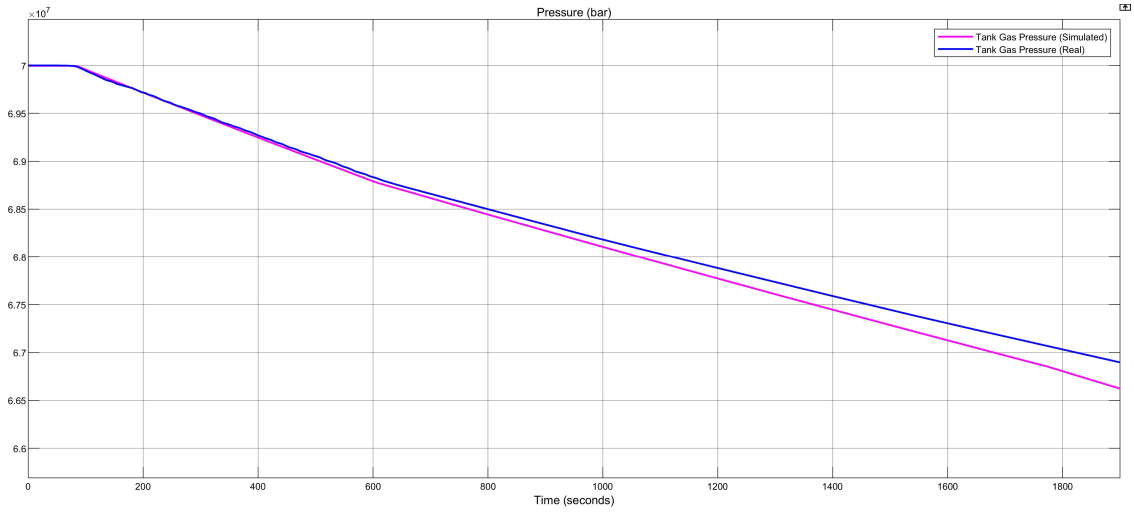

Figure 7.7. Comparison of simulated pressure data with real pressure data acquired from the vehicle.

Bibliography

[1] URL: https://www.batterytechonline.com/materials/what-is-an-intelligent-battery-sensor-.

[2] Unlock FCA Secure Gateway-protected vehicles seamlessly. URL: https://www.boschdiagnostics.com/ads-software/secure-gateway.

[3] Fuel Cell Control Unit. URL: https://www.bosch-mobility.com/en/solutions/powertrain/fuel-cell-electric/fuel-cell-control-unit/.

[4] Alternative Fuels Data Center. *How Do Fuel Cell Electric Vehicles Work Using Hydrogen?* URL: https://afdc.energy.gov/vehicles/how-do-fuel-cell-electric-cars-work.

[5] *Differences between Physical and Logical topology.* URL: https://www.computernetworkingnotes.com/networking-tutorials/differences-between-physical-and-logical-topology.html.

[6] Toyota Motor Corporation. "Toyota Mirai Technical Review". In: *Toyota Motor Corporation.* (2020). URL: https://newsroom.toyota.it.

[7] Dassault Systèmes. *Convection Heat Transfer Coefficient - SOLIDWORKS Web Help.* Accessed on March 10, 2025. 2015. URL: https://help.solidworks.com/2015/italian/solidworks/cworks/c_Convection_Heat_Coefficient.htm.

[8] dSPACE. *Hardware-in-the-Loop: The Technology for Testing Electronic Controls in Vehicle Engineering.* URL: https://www.dspace.com/en/inc/home/applicationfields/foo/hil-testing.cfm.

[9] URL: https://www.embitel.com/body-control-module-ecu-in-automotive.

[10] Etienne Rivard, Michel Trudeau and Karim Zaghib. *Hydrogen Storage for Mobility: A Review.* 2019. URL: https://www.researchgate.net/figure/Type-IV-composite-overwrapped-hydrogen-pressure-vessel-source-Process-Modeling-Group_fig1_333885192.

[11] Petronilla Fragiacomo, Matteo Genovese Francesco Piraino, Orlando Corigliano, and Giuseppe De Lorenzo. "Hydrogen-Fuel Cell Hybrid Powertrain: Conceptual Layouts and Current Applications". In: *MDPI* (2022). URL: https://www.researchgate.net/figure/Fuel-Cell-Hybrid-Electric-Vehicle-Configuration-with-Fuel-Cell-and-Battery-Energy_fig5_365793148.

[12] Ibrahim Dincer G. Kubilay Karayel. "Hydrogen storage and refueling options: A performance evaluation". In: *Elsevier* Volume 191, Part B (2024). URL: https://www.sciencedirect.com/science/article/pii/S0957582024011303.

[13] Jinwu GAO, Yunfeng HU Meng LI, Hong CHEN, and Yan MA. *Challenges and developments of automotive fuel cell hybrid power system and control*. 2019. URL: http://scis.scichina.com/en/2019/051201.pdf.

[14] Y. Liu, Q. Chen, L. Zhao, Z. Wang, X. Zhang, G. Chen, T. Li, and C. Zhang. "Hydrogen storage technologies: A comprehensive review on current status, challenges, and future directions". In: *Energy* 295 (2024). URL: https://www.sciencedirect.com/science/article/pii/S0957582024011303.

[15] Matthew M. Mench. *Fuel cell engines*. 2008. URL: https://www.academia.edu/35705116/Fuel_Cell_Engines_Mench_2008_pdf.

[16] Metatron S.p.A. *M-H70-20 Pressure Regulator for H2 Fuel Cell Vehicles*. https://www.metatron.it/it/prodotti/h2-fuel-cell-vehicle/regolatori-di-pressione/m-h70-20. 2025.

[17] *NIST Chemistry WebBook*. 2021. URL: https://webbook.nist.gov/cgi/fluid.cgi?T=313&PLow=20&PHigh=700&PInc=680&Digits=5&ID=C1333740&Action=Load&Type=IsoTherm&TUnit=K&PUnit=bar&DUnit=mol%2Fl&HUnit=kJ%2Fmol&WUnit=m%2Fs&VisUnit=uPa*s&STUnit=N%2Fm&RefState=DEF.

[18] Marina Ronchetti. *Celle a combustibile Stato di sviluppo e prospettive della tecnologia*. URL: https://www2.enea.it/it/Ricerca_sviluppo/documenti/ricerca-di-sistema-elettrico/celle-a-combustibile/rse180.pdf.

[19] M. Ruth and P. et al. Jadun. *Hydrogen Storage System Cost Analysis*. Tech. rep. NREL/TP-5400-78694. National Renewable Energy Laboratory (NREL), 2020. URL: https://www.osti.gov/biblio/1975554.

[20] AMAT Srl. *Complete Catalog*. Accessed on March 10, 2025. URL: https://www.amatsrl.it/pdf/amat_catalogo.pdf.

[21] Torbjörn Thiringer Tatiana Santos Andrade. "Low platinum fuel cell as enabler for the hydrogen fuel cell vehicle". In: *Journal of Power Sources* (2024). URL: https://www.sciencedirect.com/science/article/pii/S0378775324000910.

[22] Bernie Thompson. "Understanding Controller Area Network". In: *Motor MAgazine* (2008). URL: https://www.motor.com/magazine-summary/understanding-controller-area-networks/.

[23] Y. Zhao, L. Wang, and H. Chen. "Thermodynamic Analysis of the Emptying Process of Compressed Hydrogen Tanks in Fuel Cell Vehicles". In: *International Journal of Hydrogen Energy* 45.7 (2020), pp. 4496–4507. URL: https://www.researchgate.net/publication/330163225_Thermodynamic_analysis_of_the_emptying_process_of_compressed_hydrogen_tanks.